Computers and Structures 286 (2023) 107110

Contents lists available at ScienceDirect

Computers and Structures

journal homepage: www.elsevier.com/locate/compstruc

Uncertainty quantification and propagation in the microstructure-sensitive prediction of the stress-strain response of woven ceramic matrix composites

Adam P. Generale [a], Surya R. Kalidindi [a,b,*]

[a] George W. Woodruff School of Mechanical Engineering, Georgia Institute of Technology, Atlanta, GA 30332, USA
[b] School of Computational Science and Engineering, Georgia Institute of Technology, Atlanta, GA 30332, USA

ARTICLE INFO

Article history:
Received 3 March 2023
Accepted 27 June 2023

Keywords:
Machine learning
Bayesian inference
Multiscale modeling
Scale-bridging
Statistical calibration
Uncertainty quantification

ABSTRACT

Hierarchical multiscale modeling of heterogeneous materials has traditionally relied upon a deterministic estimation of constitutive properties when making microstructure-sensitive predictions of effective response at each subsequent length-scale. Such an approach is wholly unsuitable for a variety of material classes, such as ceramic matrix composites, which exhibit large variability at multiple length-scales. This work demonstrates a framework for approaching two open problems towards improved microstructure-sensitive predictions, namely, (i) probabilistically calibrating complex constitutive models at the mesoscale to sparsely observed macroscale experimental data, and (ii) propagating this stochastic constituent behavior at the mesoscale towards low-cost homogenized predictions for unseen microstructures. The proposed stochastic scale-bridging framework displays a continuity of information flow where no portion of the experimental data is neglected out of convenience, facilitating the greatest information gain from oftentimes costly experiments. In this paper, suitable protocols were developed to address the challenges described above. The protocols were subsequently demonstrated on ceramic matrix composite's uniaxial tensile stress–strain response, where constituent behavior at the mesoscale was described using continuum damage mechanics, and predictions encapsulating constitutive model parameter uncertainty were made for novel microstructures. The methodology presented in this work is broadly applicable to various material classes and constitutive models with high-dimensional parameter sets.

© 2023 Elsevier Ltd. All rights reserved.

1. Introduction

Ceramic-matrix composites (CMCs) using textile architectures are of tremendous interest for a variety of high-temperature structural applications [1–4]. The use of textile architectures offers an extremely large design space for the optimization of the component performance through varied stitching patterns (e.g., weaving, braiding, knitting) [5,6] and the selection of different constituent fiber and matrix materials. This large design space offers tremendous choice in the selection of combinations of effective properties [7]. However, due to the inherent variability in the multiple manufacturing steps involved, CMCs often exhibit significant stochasticity in their effective properties/performance [7–9]. This stochasticity in performance arises from both the variability in the properties of the CMC constituents (e.g., variability in the local properties of the matrix and the fibers) and the variability in their complex microstructures (caused by variability in the processing steps such as the preform production and final densification) [10]. In order to formally explore the large CMC design space within the component design process, it is necessary to develop rigorous and efficient computational schemes that can predict their effective properties as a function of the constituent properties and the microstructure, while accounting for their stochasticity. Historically, this task has been addressed primarily through extensive experimental testing campaigns that estimated parameters associated with classical phenomenological models of the material's effective properties. However, these traditional approaches incur inordinate cost as one typically needs to test a large number of permutations of weave architectures, processing histories, and multiple loading conditions.

Traditional efforts to model the performance of CMCs have largely leveraged approaches that replicate their observed nonlinear behavior, including the modeling of discrete crack formation through fracture mechanics [11], effective fracture processes

* Corresponding author at: George W. Woodruff School of Mechanical Engineering, Georgia Institute of Technology, Atlanta, GA 30332, USA.
E-mail address: surya.kalidindi@me.gatech.edu (S.R. Kalidindi).

https://doi.org/10.1016/j.compstruc.2023.107110
0045-7949/© 2023 Elsevier Ltd. All rights reserved.

through continuum damage mechanics (CDM) [12–14], and extensions incorporating viscous behavior [15,16] and/or plasticity [17]. CDM models have been particularly attractive because of their computational tractability in modeling the accumulation of damage in a continuum sense, enabling a homogenized consideration of the lower length-scale damage processes such as matrix cracking, interface debonding, and fiber fracture [14,18–20]. However, such models employ large numbers of parameters that require calibration to experimental measurements [14,21,22]. In such a high-dimensional parameter space, over-parameterized models with limited experimental data are known to provide nonunique solutions [23]. While these models applied at the macroscale show potential in the modeling of effective material response, they do so at the expense of the abstraction of various micro-scale phenomena, representing a significant simplification of material behavior. Higher resolution modeling approaches in which various length-scales of the microstructure are explicitly modeled in a finite element (FE) framework (often through the use of representative volume elements (RVEs)) open new avenues for a greater understanding of the evolution of the underlying physical processes. This explicit modeling of microstructural constituents enables a linkage between processes occurring in individual constituents and their effect on homogenized properties, providing valuable information for the design of materials. Detrimentally, this higher expressivity comes at the cost of greatly expanding microstructure uncertainty alongside the model parameter space required to predict constitutive behavior, only further compounding the issues of identifiability mentioned earlier. In prior literature, this coupled problem is often addressed by preferentially emphasizing the importance of rigorously determining the RVE domain[1], while identifying constituent behavior through experimental testing of individual constituents [26–30]. This method of constituent property assignment in the RVE implicitly assumes a similarity in constituent behavior regardless of the multimodality of the stress state, such that potentially significant error is propagated through the constituent properties even after much attention has been placed towards minimizing error associated with the microstructural domain.

The simulation computational cost for effective properties which depend upon higher order spatial statistics of the microstructure, such as high-cycle fatigue, ductility, or damage can potentially be exceedingly high, presenting computational challenges when a multitude of loading conditions must be evaluated [25,31]. A related concept is that of a statistical volume element (SVE) which samples the distributed microstructural attributes of a particular material system, significantly reducing the domain size required, and enabling the evaluation of the effective properties of the RVE through the use of an ensemble of SVEs [25,31]. As such, the use of SVEs provides a promising method for the exploration of the microstructural space and the attendant combinations of effective properties.

The robust prediction of CMC response requires an adequate understanding of both stochasticity in constituent properties alongside stochasticity in their microstructure. Towards this end, prior work has leveraged Bayesian inference [32–35] in the uncertainty quantification (UQ) of mechanical model parameters for simple macroscale models, such as the identification of the effective elastic constants in an aluminum alloy [36], a polymeric material embedded in glass [29], and laminate composites [37,38]. More complex constitutive models have also been explored while neglecting the effects of microstructure, such as the one-dimensional Von-Mises plasticity model with strain hardening [39,40], viscoelasticity [41–43], viscoplasticity [44], and viscous-damage models [45,46]. Uncertainty has also been investigated at multiple length-scales in composites through more traditional means, such as sensitivity analyses [47], or the propagation of discrete samples [48,49]. It should be highlighted that the number of parameters explored in these works are significantly lower than those used in the scale-bridging microstructure-sensitive models needed for the reliable predictions of effective properties of heterogeneous material systems. In recent work, the uncertainty in the description of the constitutive parameters in crystal plasticity models was quantified and propagated to specialized classes of preferentially oriented microstructures observed in additively manufactured samples [50]. A rigorous framework that generalizes these approaches to complex constitutive responses of RVEs/SVEs is critically lacking.

Statistical descriptors of microstructure arise from the treatment of microstructures as instantiations of a stochastic process that could be defined using the framework of n-point correlation functions [51–56]. The main concept underlying this framework is that the salient details of a microstructure controlling its effective properties are indeed captured in the n-point spatial correlations. It is further argued that the stochasticity of the microstructure is adequately captured by an ensemble of SVEs produced from a subset of specified n-point spatial correlations (usually extracted from the microstructure images obtained from the physical samples of interest). Named the Materials Knowledge Systems (MKS) [57–59], this approach has enabled the formulation of various Structure–Property (SP) linkages through the use of machine-learned surrogate models linking statistical descriptors of a microstructure to its effective properties [60–65]. Importantly, these low-cost SP linkages enable rapid exploration of the microstructural space and are particularly attractive for use in the accelerated design of novel materials [51,66,67]. While inherently encapsulating microstructure uncertainty through these advanced statistical descriptors, the SP linkages produced have largely assumed complete certainty regarding underlying constituent behavior at lower length-scales through the deterministic assignment of their properties. As such, this approach continues to fall short of the stated goal of uncertainty quantification in microstructure-sensitive constitutive modelling of heterogeneous material systems. Such SP linkages can only be created through a comprehensive understanding of both the inherent constituent and microstructural stochasticity, conditioned upon available macroscale experimental data. The challenges involved are compounded by the small experimental datasets typically available in the development of advanced material systems, such as woven CMCs.

The primary focus of this work is to resolve the numerous stated challenges in the stochastic scale-bridging for establishing low-cost probabilistic microstructure-sensitive predictions of effective properties. Towards this end, an experimental dataset consisting of five macroscale stress–strain responses of 8-ply stack of 8-harness satin SiC/SiC CMCs densified through chemical vapor infiltration (CVI), and two microstructural scans performed through micrometer resolution X-ray computed tomography (μCT) are utilized. This very limited experimental dataset is ideal for demonstrating the power and versatility of the framework proposed in this paper. The homogenized behavior of fiber bundles, or tows, and matrix material (encompassing residual macroscale porosity from CVI processing) were modeled through the use of an orthotropic CDM model defined as an Abaqus/Explicit user-defined material model (VUMAT) applied to stochastic virtual SVEs. The specific CDM model explored in this study had 13 parameters. The posterior of these CDM model parameters was establishing by devising and applying a number of novel workflows, including (i) Bayesian inference of high-dimensional CDM model parameters

[1] Defined to be the smallest domain in which the distribution of effective response does not change with the location of sampling from the larger ensemble, or increasing the size of the domain [24,25].

of the microstructure constituents, conditioned upon the limited set of available macroscale stress–strain curves, (ii) a three-step update framework to reduce the extremely high-dimensionality of the problem through a probabilistic decoupling of the CDM model parameter space and hierarchical reduced-order SP linkages accounting for all sources of uncertainty dictating the effective response of the microstructure, (iii) propagation of all available experimental data towards low-cost probabilistic microstructure-sensitive predictions, and (iv) direct tracking of all informative information from macroscale experimental data through to mesoscale property identification, and back to macroscale performance of varied microstructures.

2. Background

2.1. Continuum damage model

The damage processes occurring at varied length-scales in CMCs during progressive loading result in multiple energy dissipating mechanisms such as matrix cracking, interface debonding, sliding at the fiber/matrix interface, and fiber fracture [7,13]; all of these mechanisms contribute to their overall damage tolerance and nonlinear behavior. As previously mentioned, CDM models have historically been an attractive method for the mathematical modeling of the CMC mechanical behavior [14,18,21,22], and have been adopted in this work. The CDM model utilized in this work is a variant of that presented by Chaboche et al. [68], originally created for application to brittle materials and CMCs. It is an orthotropic CDM model which utilizes scalar damage variables $\{d_1, d_2, d_3\}$, alternatively referred as d_α with damage mode index $\alpha = \{1, 2, 3\}$, associated with the principal axes of the orthotropic material. This model simplification implies that the principal directions of damage are aligned with the axes of anisotropy describing the orthotropic material behavior, an assumption extensively applied in similar works in current literature on CMCs [68–71]. A thermodynamic potential such as the Helmholtz free specific energy potential can be defined as a function of an observable state variable, ε, and a latent internal damage variable, d_α.

$$\psi = \psi(\boldsymbol{\varepsilon}, d_\alpha) \tag{1}$$

From Eq. (1) a thermodynamic force associated with the damage variable d_α can be defined as

$$Y_\alpha = -\rho \frac{\partial \psi}{\partial d_\alpha} = -\frac{1}{2}\boldsymbol{\varepsilon} \cdot \frac{\mathbb{C}(d_\alpha)}{\partial d_\alpha}\boldsymbol{\varepsilon} \tag{2}$$

where $\mathbb{C}$ is the fourth-order stiffness tensor, ρ is the material density, and Y_α can be seen to represent the specific strain-energy release rate, in an analogous form to the energy release rate of classical fracture mechanics [72]. To satisfy the Clausius–Duhem inequality, energy dissipation through damage must be positive (i.e., $Y_\alpha \dot{d}_\alpha \geqslant 0$). As Y_α is always defined to be a positive quantity (through Eq. (2) and required softening with increasing damage), this requires that $\dot{d}_\alpha \geqslant 0$. Damage evolution is often defined in an integrated form as a monotonically increasing function to satisfy such thermodynamic constraints. A Weibull form of this integrated evolutive equation is particularly attractive as it accounts for saturation effects commonly observed in CMCs [22]. It is defined as

$$d_\alpha(t) = 1 - \exp\left[-\left\langle \frac{Y_\alpha(t) - Y_\alpha(0)}{b_\alpha} \right\rangle^{n_\alpha}\right] \tag{3}$$

where $Y_\alpha(t) = \sup_{\tau \leqslant t} Y_\alpha(\tau)$ defines the highest strain energy release rate attained in the loading history [14,21,22], $Y_\alpha(0)$ specifies the initial threshold strain energy release rate for the initiation of damage, $\langle\cdot\rangle$ the Heaviside function, and n_α and b_α denote material parameters. $Y_\alpha(0)$ is initialized as $X_{T\alpha}^2/2E_\alpha$, where E_α denote the orthotropic elastic moduli and $X_{T\alpha}$ is the uniaxial strength in tension. The method of strain equivalence [73] is leveraged to identify a transformation between the current stress tensor $\boldsymbol{\sigma}$ and an effective stress tensor $\tilde{\boldsymbol{\sigma}}$ defining the equivalent stress that would need to be applied to the undamaged material to obtain the same strain tensor. Under this assumption, this mapping is conventionally performed through a fourth-order damage operator $\mathbb{M}(d_\alpha)$

$$\tilde{\boldsymbol{\sigma}} = \mathbb{M}(d_\alpha)\boldsymbol{\sigma}. \tag{4}$$

The method of strain energy equivalence is used in order to define the form of $\mathbb{M}(d_\alpha)$, in its diagonal form in the principal coordinate system of $\boldsymbol{d}$, using Voigt notation as

$$\mathbb{M}(d_\alpha) = \begin{bmatrix} 1-d_1 & 0 & 0 & 0 & 0 & 0 \\ 0 & 1-d_2 & 0 & 0 & 0 & 0 \\ 0 & 0 & 1-d_3 & 0 & 0 & 0 \\ 0 & 0 & 0 & \sqrt{(1-d_2)(1-d_3)} & 0 & 0 \\ 0 & 0 & 0 & 0 & \sqrt{(1-d_1)(1-d_3)} & 0 \\ 0 & 0 & 0 & 0 & 0 & \sqrt{(1-d_1)(1-d_2)} \end{bmatrix}. \tag{5}$$

The modification of the undamaged compliance tensor $\mathbb{S}_0$ is then expressed as

$$\mathbb{S}(d_\alpha) = \mathbb{M}^{-1}(d_\alpha)\mathbb{S}_0\mathbb{M}^{-1}(d_\alpha). \tag{6}$$

The constitutive response of both constituents of the woven composite are prescribed using the CDM model described above. Further, it was assumed that both constituents, namely, the tows and the effective matrix (encompassing residual porosity from the CVI process), exhibit transverse isotropy. The axis of transverse symmetry for the tows was assumed to be along the tow longitudinal axis, while that for the effective matrix was assumed to be the out-of-plane direction of the composite. The effective matrix was modeled in this manner owing to the defect structures commonly observed in the matrix of CMCs, resulting in deviations from isotropic behavior [74]. As a result, the complete list of model parameters requiring calibration for the composite SVE is the 12-dimensional vector, $\boldsymbol{\theta} = \{X_{t1}^t, n_1^t, b_1^t, X_{t2/3}^t, n_{2/3}^t, b_{2/3}^t, X_{t1/2}^m, n_{1/2}^m, b_{1/2}^m, X_{t3}^m, n_3^m, b_3^m\}$, where superscripts refer to tows (t) or effective matrix (m), and subscripts refer to a specific damage mode index.

2.2. Bayesian inference of model parameters

The procedure for estimating model parameters given noisy observations is formally known as the inverse problem [75,76] [2]. The governing statistical model in this procedure is defined as

$$y^E = y^M(\boldsymbol{\theta}) + \xi \tag{7}$$

where y^E denotes the noisy observational data, y^M the predictive model with unknown parameters $\boldsymbol{\theta}$, and ξ the unknown observational noise. Directly calculating the inverse of the predictive model given y^E is generally intractable in practice, limiting the methods of identifying $\boldsymbol{\theta}$ which best matches the experimental data to model predictions. The CDM model used in this work, when applied to mesoscale constituents in an SVE, is sufficiently flexible to model highly variable homogenized nonlinear material behavior, at the cost of increased model parameterization. This high-dimensional parameterization presents significant challenges in the identification of $\boldsymbol{\theta}$, especially given sparse experimental data. It is precisely this scenario in which Bayesian approaches become increasingly useful in their ability to treat model parameters as stochastic variables exhibiting a distribution of feasible values, rather than provid-

[2] Alternatively referred to as Bayesian calibration [77], probabilistic inversion [23], or Calibration under Uncertainty (CUU) [78].

ing a deterministic result. The application of Bayes' theorem to this problem is commonly expressed as

$$p(\boldsymbol{\theta} \mid y^E) = \frac{p(y^E \mid \boldsymbol{\theta})p(\boldsymbol{\theta})}{\int p(y^E \mid \boldsymbol{\theta})p(\boldsymbol{\theta})d\boldsymbol{\theta}} \tag{8}$$

where $p(\boldsymbol{\theta})$ represents the prior encapsulating incoming knowledge (i.e., initial guess) of the values of $\boldsymbol{\theta}$, $p(y^E \mid \boldsymbol{\theta})$ the likelihood of sampling the experimental observations y^E for a specific set of model parameters, and $p(\boldsymbol{\theta} \mid y^E)$ the posterior representing the updated belief on the model parameters $\boldsymbol{\theta}$ conditioned upon the experimental observations y^E. The manipulation of conditional probabilities in Eq. (8) is especially useful in cases where $p(y^E \mid \boldsymbol{\theta})$ is easy to directly compute but an analytical form for $p(\boldsymbol{\theta} \mid y^E)$ is intractable. The likelihood is often considered as Gaussian as it arises from the model in Eq. (7) through a propagation of uncertainty with the assumption of normally distributed noise ($\xi \sim \mathcal{N}(0, \sigma)$), while for a given $\boldsymbol{\theta}, y^M$ provides a deterministic output. In applications where little prior knowledge over model parameters is available, distributions with large variances are often taken for the prior to limit its influence over the posterior.

2.2.1. Affine-invariant ensemble Markov Chain Monte Carlo algorithm

The identification of the posterior multidimensional parameter distribution conditioned on the observed experimental data (from Eq. (8) was estimated through the Affine-Invariant Ensemble MCMC algorithm [79,80]. This ensemble sampler was utilized due to the expectation of multimodal behavior or skew in the posterior distribution, owing to the high-dimensionality of the parameter space. MCMC algorithms enable samples to be drawn from the posterior probability density (Eq. (8)), without computing the evidence, which is generally expensive or intractable to compute [80]. The sampling strategy of MCMC can be viewed as a method for generating a random walk in parameter space that with sufficient iterations, results in a representative set of samples from the posterior distribution. During this random walk, each individual point in the Markov chain $\mathbf{X}(t_i) = \boldsymbol{\theta}_i$ depends solely on the position of the prior step $X(t_{i-1}) = \boldsymbol{\theta}_{i-1}$. In comparison to the standard Metropolis–Hastings (M-H) algorithm, the Affine-Invariant Ensemble algorithm employs an ensemble of K walkers $S = \{\mathbf{X}_k\}$, where the proposal distribution for one of the walkers (indexed by k) is based on the locations in parameter space of the remaining $K-1$ walkers defining the complementary set of walkers $S_{[k]} = \mathbf{X}_j, \forall j \neq k$. During each iteration, the position of all walkers in the ensemble is updated. In order to update the position of a single walker at position $\mathbf{X}_k$, a walker is drawn at random from the complementary set $S_{[k]}$ and the new proposed position for the walker $\mathbf{X}_k$ can be written as

$$\mathbf{W} = \mathbf{X}_j + Z(\mathbf{X}_k(t) - \mathbf{X}_j) \tag{9}$$

with Z being a random variable drawn from the distribution $\kappa(z)$. The particular distribution recommended by Goodman and Weare [79] is

$$\kappa(z) \propto \begin{cases} \frac{1}{\sqrt{z}} & \text{if } z \in \left[\frac{1}{a}, a\right] \\ 0 & \text{else} \end{cases} \tag{10}$$

where a is a tunable parameter set to 2. The proposal walker location is then accepted with probability

$$q = min\left(1, Z^{D-1}\frac{p(\mathbf{W}}{p(\mathbf{X}_k(t))}\right) \tag{11}$$

where D is the dimensionality of the space being sampled. The proposal is then accepted or rejected when compared against a sample drawn from a standard uniform distribution $r \leftarrow R \sim \mathcal{U}[0,1]$. If $r \leqslant q$ then the transition is accepted and $\mathbf{X}_k(t+1)$ is assigned the position $\mathbf{W}$. The algorithm described above has been extensively used in astrophysics applications [81–83] where models exhibit similar high-dimensionality as the CDM model considered in this work. In such high-dimensional spaces, traditional algorithms require multiple tunable parameters (their number scaling with the problem size), whereas the Affine-Invariant Ensemble Sampler employs only one parameter [80]. It has also been shown to provide improved performance in highly skewed distributions (such as the Rosenbrock density) over the conventional M-H algorithm [79]. The specific MCMC algorithm used in this study is implemented in the python package *emcee*, developed by Foreman-Mackey *et al.* [80].

2.2.2. Support points and minimum energy distance

Due to the stochastic nature of random walks through probability space, it should be apparent that for MCMC sampling to sufficiently approximate a distribution requires an extremely large number of samples. This large collection of samples which collectively define the approximate distribution severely limits one's ability to propagate the uncertainty of complex multi-modal distributions forward in an analysis. The concept of support points defined through work of Mak and Joseph [84] allows for a method of compacting MCMC samples in Bayesian computation. Such support points represent a reduced number of points which when taken collectively minimize the energy distance between the original MCMC posterior and a compact approximate posterior distribution. The original MCMC posterior can be summarized by the dataset $\mathcal{D} = \{\mathbf{Z}_i\}_{i=1}^N \in \mathbb{R}^{N\times d}$, which are drawn from the underlying posterior distribution $\mathbf{Z}_i \sim F$. The energy distance $\mathbb{ED}$ [85] measure defines a metric for measurement of the similarity of distributions of random vectors. For $\{\mathbf{z}_i\}_{i=1}^n$ points within $\mathcal{D}$ the energy distance can be estimated as

$$\overline{\mathbb{ED}}_{n,N} = \frac{2}{nN}\sum_{i=1}^{n}\sum_{j=1}^{N}\|\mathbf{z}_i - \mathbf{Z}_j\|_2 - \frac{1}{n^2}\sum_{i=1}^{n}\sum_{j=1}^{n}\|\mathbf{z}_i - \mathbf{z}_j\|_2 - \frac{1}{N^2}\sum_{i=1}^{N}\sum_{j=1}^{N}\|\mathbf{Z}_i - \mathbf{Z}_j\|_2 \tag{12}$$

where $\|\cdot\|_2$ is the L_2 norm. The minimization of this metric results in a collection of points best representing F, known as support points [84]. Algorithms for the solution of this optimization problem are detailed in the work of Vakayil and Joseph [86] and have been employed in this work.

2.3. Feature engineering of microstructures

2.3.1. 2-Point spatial correlations

Quantification of the microstructure is performed in this work through the use of 2-point spatial correlations and the MKS framework [57–59]. This framework utilizes a voxelated representation of the SVE as an array m_s^h [57], reflecting the volume fraction of material local state h in voxel s. For describing 3-D SVEs, it is convenient to use $s = \{s_1, s_2, s_3\}$. Furthermore, as each voxel is assigned to a singular material local state, the value of m_s^h is either zero or one (otherwise described as eigen-microstructures) [57]. The strategies and protocols for computing 2-point correlations of a microstructure have been described in detail in prior literature [57,59], and can be expressed as

$$f_r^{hh\prime} = \frac{1}{|\mathbf{S}|}\sum_{\mathbf{s}}^{\mathbf{S}} m_s^h m_{s+r}^{h\prime} \tag{13}$$

where $\mathbf{S}$ denotes the set of voxels in the 3-D periodic SVE of the microstructure, and $|\mathbf{S}|$ the total number of voxels. $f_r^{hh\prime}$ can be computed efficiently using the Fast Fourier Transform (FFT) algorithm

[62,87], and serve as the initial high-dimensional set of features representing the microstructure in formulating the desired SP linkages. More specifically, $f_r^{hh\prime}$ can be visualized as a mapping between a specified vector r and a statistic that informs the probability of finding the specified local states separated by this vector in the microstructure. Consequently, in the r-space, $f_r^{hh\prime}$ can be visualized as a 3-D contour [88–90].

2.3.2. Dimensionality reduction

Principal component analysis (PCA) offers a robust dimensionality reduction method for the set of spatial correlations considered in this work [91]. This method linearly transforms the original data into a new frame that is arranged to maximize the variance captured with each orthonormal basis vector. This transformation can be mathematically described as

$$\mathbf{f}_r^{(j)} = \sum_{k=1}^{\min((J-1),R)} \alpha_k^{(j)} \boldsymbol{\varphi}_{kr} + \bar{\mathbf{f}}_r \tag{14}$$

where $\mathbf{f}_r^{(j)}$ is a vectorized representation of the spatial correlations of the jth microstructure, J is the total number of microstructures, R is the number of dimensions in the original dataset, $\alpha_k^{(j)}$ are the principal component weights (i.e., PC scores) of the jth microstructure, $\boldsymbol{\varphi}_{kr}$ is the principal components (i.e., basis vectors of the transformed space), and $\bar{\mathbf{f}}_r^{(j)}$ represents the expected value of $\mathbf{f}_r^{(j)}$ across the ensemble. The number of principal components to be retained (i.e., R) can be determined through the evaluation of the explained variance by each basis vector as a portion of the total variance in the full dataset. Prior work [90] has demonstrated that more than 90% of the variance in most microstructure ensembles is explained within the first five terms. This reduction in dimensionality without appreciable loss in representation greatly facilitates the development of high fidelity reduced-order SP models.

2.4. Sparse variational multi-output gaussian process regression

The Sparse Variational Multi-Output Gaussian Process (SVMOGP) utilized in the development of the forward surrogate model in this work is briefly described in this section, with more details presented in Appendix A.

Gaussian processes ($\mathcal{GP}$s) [92] can be viewed as probability distributions over functions, providing important properties related to Bayesian analyses [32,34]. A stochastic function can be described as a $\mathcal{GP}$, i.e., $f(\cdot) \sim \mathcal{GP}(\upsilon(\cdot), k(\cdot,\cdot'))$, which is uniquely determined through a mean function $\upsilon(\cdot)$ and a covariance function $k(\cdot,\cdot')$ parameterized by hyperparameters, $\boldsymbol{\theta}_k$. Often, the mean function is taken to be $\upsilon \equiv 0$ without loss of generality.

Given a training dataset, $\{(\mathbf{x}_n, y_n)\}_{n=1}^N$ of N corrupted observations with an assumed Gaussian noise $\xi_i \sim \mathcal{N}(0, \sigma_y^2)$ (see Eq. (7)), the collection of all training inputs can be denoted as $\mathbf{X}$, the vector of all outputs as $\mathbf{y}$, and $\mathbf{f}$ the training latent function values. The covariance function used in this work is the automatic relevance determination squared exponential (ARD-SE) [32] defined as

$$k(\mathbf{x}, \mathbf{x}') = \sigma_f^2 \exp\left(-\frac{1}{2}\sum_{n=1}^{N} \frac{(\mathbf{x}-\mathbf{x}')^\top (\mathbf{x}-\mathbf{x}')}{\lambda_n^2}\right) \tag{15}$$

where the hyperparameters, $\boldsymbol{\theta}_k$, are comprised of λ_n specifying a separate length-scale for each input dimension and σ_f the amplitude. Exact inference of a single output $\mathcal{GP}$ model can be performed through estimating the covariance hyperparameters by maximization of the log-marginal likelihood given by

$$\log p(\mathbf{y}|\mathbf{X}, \boldsymbol{\theta}_k) = -\frac{1}{2}\mathbf{y}^\top \left[\mathbf{K_{ff}} + \sigma_y^2 \mathbf{I}\right]^{-1} \mathbf{y} - \frac{1}{2}\log\left|\mathbf{K_{ff}} + \sigma_y^2 \mathbf{I}\right| - \frac{N}{2}\log(2\pi). \tag{16}$$

In small dimensional datasets, $\mathcal{GP}$ regression provides a powerful and flexible method for the learning of scalar outputs while providing uncertainty measures on its predictions. A core limitation preventing its widespread use is the necessity of computing $\left[\mathbf{K_{ff}} + \sigma_y^2 \mathbf{I}\right]^{-1}$, whose computational complexity of $\mathcal{O}(N^3)$ limits its practicality when confronted with large datasets. Sparse approximations to this Gaussian process methods aim to address this task through the use of M inducing inputs $\mathbf{Z} = \{z_m\}_{m=1}^M$ independent of X (also referred to as pseudo-inputs) resulting in cost $\mathcal{O}(NM^3)$ time for a chosen $M \leqslant N$, providing a low rank approximation to the full covariance $\mathbf{K_{ff}}$. An elegant method to accomplish this task is the Variational Free Energy (VFE) approximation [93]. The covariance function hyperparameters and inducing inputs are jointly optimized by maximizing a lower bound to the exact marginal likelihood, where the inducing input locations are selected through minimization of the Kullback–Leibler (KL) divergence (denoted as D_{KL}) between the variational $\mathcal{GP}$ and the true posterior $\mathcal{GP}$. Importantly the KL divergence provides a metric on the error of the approximation to the exact posterior solution, while the method of selecting the inducing points provides a method of regularization on the solution, avoiding overfits. This lower bound to the exact marginal likelihood can be expressed using a distribution $q(f)$ over the entire infinite dimensional function as

$$\mathcal{F}(q^*, \boldsymbol{\theta}_k) = \log p(\mathbf{y} \mid \boldsymbol{\theta}_k) - D_{KL}(q(f) \| p(f \mid \mathbf{y}, \boldsymbol{\theta}_k)) \tag{17}$$

The function values at the inducing point locations are denoted as u. The disjoint infinite dimensional function can then be represented as $f = \{u, f_{\neq u}\}$, and an approximation to the posterior is provided by $q(f) = q(u, f_{\neq u} \mid \boldsymbol{\theta}_k) = p(f_{\neq u} \mid u, \boldsymbol{\theta}_k) q(u)$. Under this approximation, $f_{\neq u}$ is only influenced through the inducing points and not the data directly. This approximate posterior simplifies the VFE bound defined in Eq. (17) to a computational complexity of $\mathcal{O}(NM^2)$. The bound can be maximized in closed form with respect to the variational posterior, resulting in an optimal q^* and an updated VFE bound which can be optimized for the identification of $\boldsymbol{\theta}_k$ as

$$\mathcal{F}(q^*, \boldsymbol{\theta}_k) = -\frac{N}{2}\log(2\pi) - \frac{1}{2}\log\left|\hat{\mathbf{K}}_{\mathbf{ff}}\right| - \frac{1}{2}\mathbf{y}^\top \hat{\mathbf{K}}_{\mathbf{ff}}^{-1}\mathbf{y} - \frac{1}{2\sigma_y^2}\mathrm{tr}(\mathbf{K_{ff}} - \mathbf{Q_{ff}}) \tag{18}$$

where $\hat{\mathbf{K}}_{\mathbf{ff}} = \mathbf{Q_{ff}} + \sigma^2 \mathbf{I}$, and $\mathbf{Q_{ff}} = \mathbf{K_{fu}} \mathbf{K_{uu}}^{-1} \mathbf{K_{uf}}$ provides the low rank approximation. For clarity, elements of the covariance matrices are calculated as $[\mathbf{K_{uu}}]_{mm'} = k(\mathbf{z}_m, \mathbf{z}_{m'})$ and $[\mathbf{K_{fu}}]_{nm'} = k(\mathbf{x}_m, \mathbf{z}_{m'})$. Predictions of the VFE model can be expanded to handle multi-output functions in a similar manner to the scalar output case, through expansion of the covariance matrix to express correlations between related outputs [94]. Such Multioutput Gaussian processes (MOGP) learn a multioutput function $f(x) : \mathcal{X} \to \mathbb{R}^P$ with the input space X being $\mathbb{R}^D$. The p-th output of $f(x)$ is expressed as $f_p(x)$, with its complete representation given as $f = \{f_p(x_i)\}_{i=1}^n$. MOGPs are similarly completely defined by their covariance function (assuming $\upsilon \equiv 0$), resulting in a covariance matrix $K \in \mathbb{R}^{NP \times NP}$. Under this scenario, the advantages of a sparse representation become increasingly apparent, reducing the complexity from $\mathcal{O}(N^3P^3)$ to $\mathcal{O}(M^3P)$ with efficient inference schemes utilizing interdomain approximations [95]. In this work, the multi-output covariance matrix is constructed through the Linear Model of Coregionalization (LMC) [94,96]. This model represents a method of constructing the multi-output function from a linear transformation $W \in R^{P \times L}$ of L independent functions $g(\mathbf{x}) = \{g_l(\mathbf{x})\}_{l=1}^L$. Each function is constructed as an independent $\mathcal{GP}$, $g_l(x) \sim \mathcal{GP}(0, k_l(\mathbf{x}, \mathbf{x}'))$, each with its own covariance function, resulting in the final expression

$f(\mathbf{x}) = \mathbf{W}g(\mathbf{x})$. The multi-output covariance function described by this model is then expressed as

$$k(\{x,p\},\{x',p'\}) = \sum_{l=1}^{L} W_{pl} k_l(\mathbf{x},\mathbf{x}') W_{p'l} \tag{19}$$

which can be seen to encode correlations between output dimensions, and due to the form of the covariance function in Eq. (19), the MOGP provides for an incredibly expressive model. The performance of the SV-MOGP model is evaluated through the Normalized Mean Absolute Error (NMAE) metric for each output dimension, defined as

$$NMAE_p = \frac{1}{N}\sum_{i=1}^{N} |y_{pi} - f_p((\mathbf{x}))| / \bar{\mathbf{y}}_p \tag{20}$$

where $f_p(\mathbf{x})$ is the predicted expected value for the input vector $\mathbf{x}$ at output p, and $\bar{\mathbf{y}}_p$ denotes the mean of the test output.

3. Bayesian calibration of damage model

3.1. Experimental dataset

The experimental dataset considered in this work consisted of five 8-ply stacks of 8HS SiC/SiC CVI-densified CMCs reinforced with Hi-Nicalon Type S (HNS) fiber. The samples were monotonically loaded in tension until failure with the resulting normalized stress–strain curves displayed in Fig. 1.

Additionally, two 1-inch diameter circular specimens extracted from the same panel were subjected to non-destructive evaluation (NDE) through micrometer resolution X-ray computed tomography (μCT) in order to provide details of the mesoscale microstructure, including the stochastic variability of the woven tow paths and distribution of residual macro-porosity from CVI processing. The μCT scans were segmented with a workflow developed using the MATLAB image toolbox [97,98] to separate the tow bundles from the combination of matrix and macro-porosity, before computing 2-point spatial correlations of the microstructure.

3.2. Virtual microstructure generation

An ensemble of virtual SVEs of 8-ply stacks were generated for this study with the 8HS repeating unit cell (RUC) [99]. The goals of virtual microstructure generation were (i) to produce training data covering a broad range of microstructural variations, and (ii) to produce microstructures with sufficient similarity to the two experimental scans available. The generated microstructures will enable the calibration of the CDM model damage parameters in a Bayesian uncertainty quantification framework.

The workflow used for virtual microstructure generation is presented in Fig. 2, and consisted of four main steps that were implemented utilizing the open source software TexGen [100]. Characteristic dimensions defining the microstructure were treated as random variables with Gaussian and uniform distributions such that the generation process can be viewed as entirely stochastic, outputting entirely unique microstructure instantiations. The process starts with the specification of a single ply of the RUC. Initially, the tow cross-sections are considered to be perfectly elliptical and uniform throughout the ply. The characteristic dimensions of the ellipse are sampled from the distributions defined in Table 1, which are extracted from prior work on similar material systems [101,102].

An example of a generated ply with a selected set of mean cross-section parameters (t_w and t_h) can be observed in frame 1 in Fig. 2. Subsequently, frame 2 is generated by moving the control points dictating behavior of the spline at the centroid of each tow

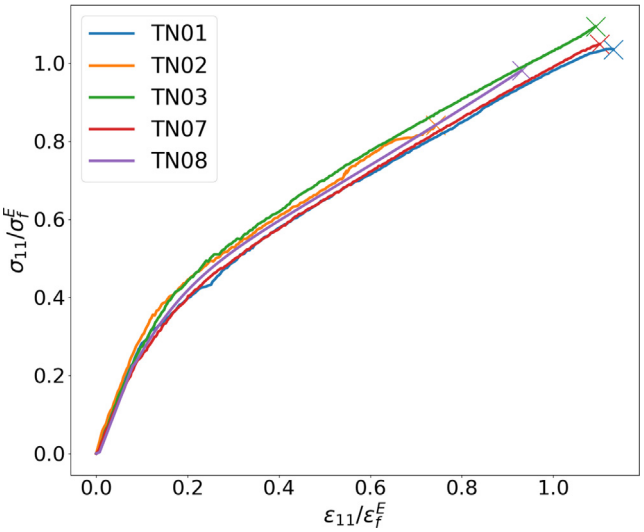

Fig. 1. Monotonic stress–strain tensile specimen responses normalized by the mean failure strain ε_f^E and the mean failure stress σ_f^E (superscript E is included to denote experimental results).

(indexed by $\beta = \{1,\ldots,9\}$), and perturbing the cross-section dimensions according to the distributions for $t_{w\beta}$ and $t_{h\beta}$ in Table 1 The tow cross-section shape is further perturbed through in-plane translations and rotations at each of the control points, and finally varied to range from a perfect ellipse to a rectangular cross-section using options in TexGen software [100]. In frame 3, the perturbation to the tow control points can be observed to follow a sinusoidal surface (defined using control parameters A, φ, ν_1, ν_2; see Table 1). This process assumes statistical independence during sampling from each of the distributions listed. The composite stack is then assembled from 8 instantiations of plies generated using the process described above. Ply shearing, in-plane and out-of-plane offsets, and ply compaction were all applied independently to each ply as per the distributions summarized in Table 1. An exemplar instantiation of an 8HS microstructure is shown in frame 4, with its corresponding voxelization shown in frame 5. Each microstructure was discretized with uniform voxels of size 200 μm $\times$ 200 μm $\times$ 40 μm. The virtual generation strategy described above was utilized to produce an ensemble of 1,500 microstructures. Each of these serves as a 3-D voxelated SVE, where each voxel is assigned to be either tow or effective matrix (i.e., two distinct local states). A FE mesh was created for each SVE by converting each voxel to an eight-noded three-dimensional continuum element with reduced integration (C3D8R elements in Abaqus [103]). The use of such voxel-based meshing enables implementation of automated workflows for data generation and surrogate model development [62,63,90,104–106]. All microstructures utilized in this work were quantified using the 2-point spatial correlations described in Section 2.3.1. For the two-constituent microstructures studied here, only one set of auto-correlations is adequate due to interdependencies in the complete set of 2-point spatial correlations [51,87]. Therefore, only the tow auto-correlations (i.e., f_r^{00}) are computed for use in this work. The number of computed auto-correlations is generally the same as the number of voxels in the SVE. In our work, we standardized the number of auto-correlations to $51 \times 51 \times 51$, producing 132,651 features for each microstructure.

Fig. 3a illustrates the 3-D tow auto-correlations for an exemplar microstructure from the generated ensemble as 2-D contours on the main orthogonal planes through the origin (i.e., $r = 0$); these aid in visual clarity compared to 3-D contours. These auto-

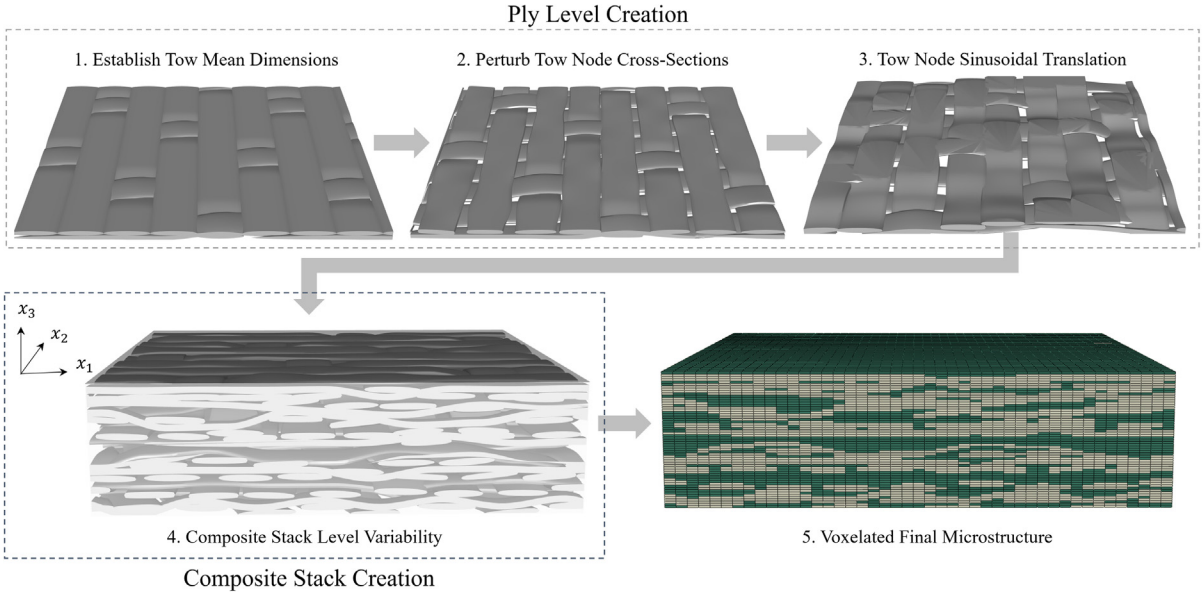

Fig. 2. Illustration of the workflow for the stochastic generation of virtual microstructures.

Table 1
Distributions utilized for sampling the geometric parameters involved in the specification of the RUC and the building of the woven SVE virtual microstructure.

Microstructural Parameter Description	Distribution
Initial Tow Major Axis (mm)	$t_w \sim \mathcal{N}(1.0301, 0.0650)$
Initial Tow Minor Axis (mm)	$t_h \sim \mathcal{N}(0.1218, 0.0061)$
Tow Point Major Axis (mm)	$t_{w\beta} \sim \mathcal{N}(t_w, 0.0650)$
Tow Point Minor Axis (mm)	$t_{h\beta} \sim \mathcal{N}(t_h, 0.0061)$
Tow Point Power	$t_{p\beta} \sim \mathcal{U}(0.1, 1.0)$
Tow Point Rotation (deg)	$t_{r\beta} \sim \mathcal{N}(-2.0, 2.0)$
Tow Point In-Plane Translation (mm)	$\begin{bmatrix}\Delta x_1\\ \Delta x_2\end{bmatrix} \sim \mathcal{N}\left(\boldsymbol{0}, \begin{bmatrix}0.075\\ 0.075\end{bmatrix}\right)$
	$A \sim \mathcal{U}(-0.15, 0.15)$
Tow Point Out-of-Plane Translation Parameters	$\boldsymbol{\phi} \sim \mathcal{U}(-\frac{\pi}{2}, \frac{\pi}{2})$
	$v_1, v_2 \sim \mathcal{U}(0, 0.5)$
Ply Shear Angle (deg)	$p_s \sim \mathcal{N}(-8, 8)$
Ply Compaction (%)	$p_c \sim \mathcal{U}(0.01, 0.25)$

correlations are denoted as f_r^{00} (the superscript 0 refers to the tow material state); the value at $r = 0$ corresponds to the tow volume fraction. Patterns seen in the f_r^{00} contours can be directly linked to physical features in the microstructure. For example, the repeating striations of peaks observed in the $X - Z$ and $Y - Z$ planes reflect the mean spacings between the plies (controlled by p_c in Table 1). Much richer features are seen in the $X - Y$ plane due to the much more complex geometry of the weave in this plane. The peaks in the $X - Y$ plane reflect the spacings between the overlapping points between the warp and weft directions, which reflect locations of higher probability of finding tow voxels. Perturbations in the intensity of these tertiary peaks are a direct result of the stochastic generative process, with $t_{w\beta}$ and $t_{h\beta}$ adjusting the local tow to tow spacing, Δx_1 and Δx_2 translating tow control points locally in-plane, and p_s applying ply shearing. The sum total of these stochastic perturbations results in a dissipation of these tertiary peaks, further decreasing with distance from the position $r = 0$. Secondary peaks can also be observed to follow a rotated ellipse surrounding the origin, which can be correlated to the relative positions of cross-over points in the 8HS RUC architecture. For more information regarding the interpretation of 2-point spatial auto-correlations in woven composites and their relation to features of the microstructure, the reader is referred to our prior work on this topic [107]. PCA is used in this work to obtain a low-dimensional representation of the tow auto-correlations for the full ensemble of generated microstructures. The PC basis was established through the tow auto-correlations of the 1,500 virtually generated microstructures and 2 μCT experimental microstructures. $X - Y$ and $X - Z$ sections of the first three PC bases passing through the origin are shown in Figs. 3b and 3c, respectively. Inspection of these basis maps illustrates that the first PC basis, $\boldsymbol{\varphi}_{1r}$, captures primarily volume fraction information. Additionally, $\boldsymbol{\varphi}_{1r}$ appears to capture salient short-range perturbations in the overlapping points of the woven architecture, evidenced by larger peaks immediately surrounding the origin in the $X - Y$ section. The influence of weaker long-range perturbations can also be seen at the distance of the 8HS RUC cross-over points. The second PC basis, $\boldsymbol{\varphi}_{2r}$, predominately captures mid-range perturbations surrounding the origin, as evidenced by the rotated elliptical collection of peaks in the $X - Y$ plane and the shift in correlation distance in the $X - Z$ plane. The particularly strong band of peak values through the origin of the $X - Y$ plane for this basis allows the quantification of the sinusoidal perturbations of the plies within the microstructure. The third PC basis, $\boldsymbol{\varphi}_{3r}$, appears to capture yet longer-range phenomena in the composite stack, alongside details of ply shearing. It should be noted that each PC basis here represents a set of 132,651 spatial statistics, and as such, their precise interpretation is challenging. The computed tow auto-correlations for the entire ensemble of generated microstructures and the two experimental μCT scans (denoted as T31-B1 and T41-B1) are projected into the first two principal bases in Fig. 4. The $X - Z$ cross-sections of select microstructures are shown to provide additional confirmation regarding the ability of the PC bases in differentiating microstructures within the ensemble. Three microstructures were specifically selected to illustrate the roles of PC scores α_1 and α_2. Microstructures #898 and #972 are mainly different in their values of α_2. Comparison of these microstructures indicates that lower values of α_2 correspond to higher values of sinusoidal perturbation of the plies. Similarly, a comparison of microstructures #645 and #972 suggests that larger values of α_1 correspond to higher tow volume fractions. Fig. 4 also highlights that the distribution of generated microstructures is much more asymmetric in α_2 in comparison to α_1. This is because the sinusoidal perturbations would naturally be limited by

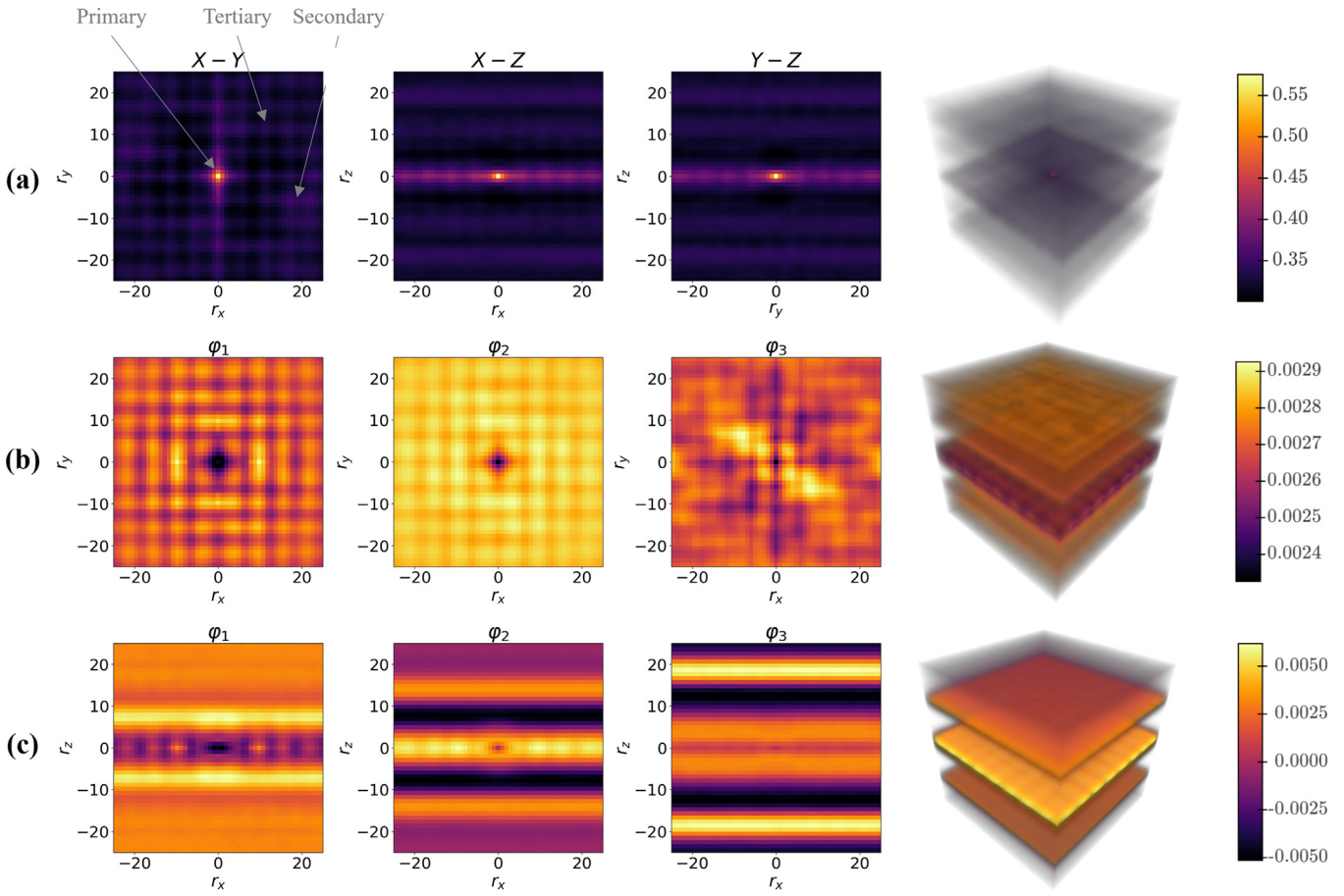

Fig. 3. Exemplar spatial correlations along with PC bases. (a) Orthogonal sections passing through the origin from an exemplar set of computed 3-D tow auto-correlations, (b) $X-Y$ sections passing through the origin for the first three PC bases, $\boldsymbol{\varphi}_{1:3r}$, (c) $X-Z$ sections passing through the origin for the first three PC bases, $\boldsymbol{\varphi}_{1:3r}$.

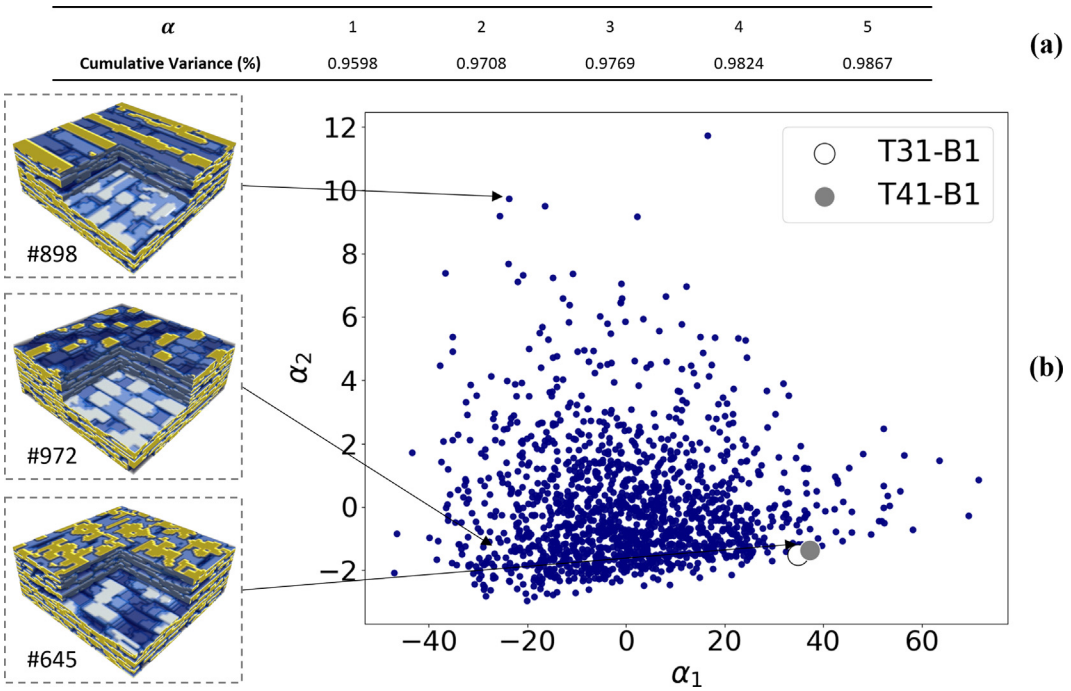

Fig. 4. Principal component representations of the ensemble of microstructures studied along with exemplar microstructures. (a) Cumulative explained variance with increasing number of principal components, and (b) projected view of the virtually generated microstructure ensemble and the two experimental microstructures in the PC subspace spanned by $\boldsymbol{\varphi}_{1r}$ and $\boldsymbol{\varphi}_{2r}$.

increasing ply compaction, thus making it difficult to generate microstructures that are both compacted and exhibit high levels of sinusoidal perturbations. Note that these characteristics of the generated ensemble are captured naturally by the unsupervised feature engineering protocols employed in our work. The statistical characterization using spatial auto-correlations enables a robust method of differentiating microstructures, and identifying virtually generated structures demonstrating the most similarity to the two experimental scans. The efficiency of PCA in providing low-dimensional representations can be seen in Fig. 4b, displaying the explained variance of the first five basis vectors, where greater than 98% is explained within the first four PC scores. While the vast majority of variance is explained within the first few PCs, prior work has demonstrated improvements in the accuracy of surrogate models built with larger sets of PC scores [65,88,89,108–110].

3.3. Finite element model

Effective tensile uniaxial stress–strain response of various SVEs considered in the microstructure ensemble were determined through the use of the CDM model (described in Section 2.1) implemented through a VUMAT user subroutine in the commercial FE solver Abaqus/Explicit [103]. In the CDM model considered, Eq. (3) provides mechanistic regularization ameliorating issues of mesh dependence in the FE implementation [111]. During implementation this was verified through a mesh dependence study on a simple hole in plate test sweeping from 2,154–600,420 elements with convergence in force–displacement curves throughout loading. This regularization aids in addressing the formation of localization bands, and prevents such continuous bands from reaching the scale of the SVE. Inertial effects were found to be minimal and less than 0.5% of the strain energy during progressive loading past an absolute strain of 0.1%, inducing minimal error on the solution by use of this solver. Perfect contact between voxels associated with the two local states were considered in the model as frictional forces occur at a lower length-scale in the material hierarchy, namely, the individual fiber/interfacial level for which energy dissipation processes are modeled approximately through the CDM model. Loading was applied for all SVEs through a relative displacement of 0.11 mm in the x_1-direction imposed across the SVE as periodic boundary conditions [112,113]. Similar approaches have been extensively applied in prior literature in the calculation of effective properties of SVEs [114–116]. First-order homogenization of the effective strain, stress, and specific strain-energy release rate were computed as

$$\overline{\boldsymbol{\sigma}} = \frac{1}{|\mathbf{S}|}\int \boldsymbol{\sigma} d\,|\,\mathbf{S}\,|,\ \overline{\boldsymbol{\varepsilon}} = \frac{1}{|\mathbf{S}|}\int \boldsymbol{\varepsilon} d\,|\,\mathbf{S}\,| \tag{21a}$$

$$Y_{\alpha}^{\beta} = \frac{1}{\mathbf{T}^{\beta}}\int Y_{\alpha} d\mathbf{T}^{\beta} \tag{21b}$$

where the volume averages for stress and strain are performed over the entire SVE, and the volume average for the strain-energy release rate is performed over a specific subset of tows (this volume is denoted as $\mathbf{T}^{\beta}$). For the voxelated meshes used in this study, the volume averages are replaced by simple averages over the respective sets of integration points. While the specified integrated damage evolution of the CDM model in Eq. (3) is able to account for damage saturation effects, it results in slow and incremental material softening where explicit consideration of individual cracks is not considered. This behavior precludes an adequate modeling of rapid failure of the SVE. As such, in order to determine a predicted failure strain from the FE simulations, it was assumed that the failure was driven by rapid fracture of tows oriented predominantly in the loading direction as a non-local failure criterion. Following classical Fracture Mechanics approaches, material failure in our study was defined by a critical value of the longitudinal strain-energy release rate in the tows, Y_1 (see Eq. (2)), denoted as Y_{1C} [117]. Y_{1C} is thus incorporated as an additional model parameter into $\boldsymbol{\theta}$. With the 8HS architecture and each SVE consisting of an 8-ply stack, an average of the 64 tows oriented in the loading direction were continuously evaluated during progressive loading. This procedure resulted in strain-energy evolution curves described by the quantity $\overline{Y}_1^M = \mathbb{E}[Y_1^{\beta}]$; the results for an exemplar microstructure are presented in Fig. 5.

This particular CDM model and the micromechanical failure criterion implicitly present several limitations related to modeling the behavior of CMCs. Specifically, the CDM model as implemented does not exhibit coupling in damage evolution between various damage modes, a phenomena readily observed in sequential multiaxial loading [68,118], precluding the capture of loading path dependency with a specified form for damage evolution. Viscous effects are also neglected, alongside the accumulation of residual strain from internal fiber failures. In composites which exhibit lower contrast in elastic properties on orthotropic planes of symmetry, the use of scalar damage variables associated with these planes may also prove to be limiting. While the simple micromechanical failure criterion has demonstrated success in the prediction of failure in CMCs [119] and polymer matrix composites [120,121], it similarly demonstrates its own limitations, including challenges in identifying the intrinsic length-scale over which Eq. (21b)) is to be taken.

3.4. Three-step Bayesian framework

The main goal of this work is to demonstrate a novel Bayesian framework for the microstructure-sensitive predictions of effective tensile stress–strain curves and the strain to failure while accounting for uncertainty in the available experimental data (across both the stress–strain responses as well as the microstructural domain). Towards this goal, the uncertainty in the experimental measurements needs to be propagated to the underlying CDM model mesoscale parameters. In this study, this challenge is accomplished by extending the previously developed Bayesian framework [38,122] and formulating a novel three-step Bayesian framework. In the first step, a surrogate model is built to capture the relationship between the material microstructure and its effective mechanical response, while explicitly considering all of the unknown CDM parameters as regressors. In the second step, a posterior is established on the unknown model parameters using the available, and often limited, experimental dataset. This process often needs to account for the uncertain or incomplete information of both the material microstructures and their measured stress–strain responses. The final step combines the results from both prior steps, in marginalizing out the uncertainty of the model parameters to provide microstructure-sensitive probabilistic predictions for new microstructures. This three-step workflow is sufficiently general and can be applied to varied combinations of microstructural classes and material physics (i.e., constitutive models) of interest. In the present work, our focus will be exclusively on the CDM model introduced in Section 2.1 for modeling the nonlinear behavior of continuous fiber reinforced 8HS CMCs. The microstructure-sensitive probabilistic prediction of tensile stress–strain curves for new composite microstructures could be expressed as

$$p(\boldsymbol{\sigma}^M, \varepsilon_f^M \mid \boldsymbol{\alpha}, \boldsymbol{\sigma}^E, \varepsilon_f^E, \boldsymbol{\alpha}^E) = \int p(\boldsymbol{\sigma}^M, \varepsilon_f^M \mid \boldsymbol{\theta}, \boldsymbol{\alpha}) p(\boldsymbol{\theta} \mid \boldsymbol{\sigma}^E, \varepsilon_f^E, \boldsymbol{\alpha}^E) d\boldsymbol{\theta} \tag{22}$$

where $\boldsymbol{\sigma}^E \in \mathbb{R}^N$ represents a discretized vector of N experimentally measured stress values corresponding to $\boldsymbol{\varepsilon} \in \mathbb{R}^N$ denoting a prescribed vector of N strain values (usually taken to be uniformly dis-

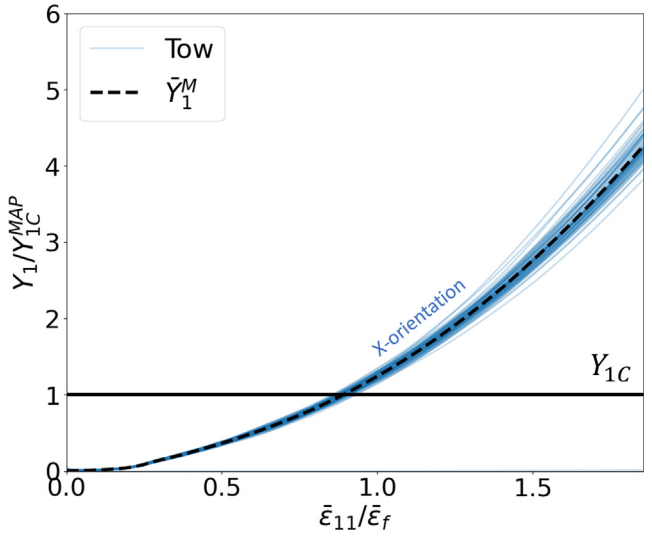

Fig. 5. Evolution of strain-energy release rate as a function of the imposed macroscale strain. The lighter blue lines present the evolution of Y_1 for individual tows (normalized by the inferred MAP value of Y_{1C}, denoted as Y_{1C}^{MAP}), while the darker dashed line presents the volume averaged response in the longitudinal tows (parallel to the loading direction).

tributed over the desired range of strain values), $\boldsymbol{\varepsilon}_f^E$ denotes the experimentally measured failure strain, $\boldsymbol{\alpha}^E$ the vector of PC scores quantifying the microstructures obtained from μCT experimental scans, $\boldsymbol{\varepsilon}$ is the vector of PC scores quantifying the new microstructure for which predictions are to be made, and $\boldsymbol{\theta}$ denotes the vector of CDM parameters introduced in Section 2.1. $\boldsymbol{\sigma}^M$ and ε_f^M represent similar quantities as $\boldsymbol{\sigma}^E$ and ε_f^E, but from model predictions. Importantly, Eq. (22) implicitly assumes that the constituent material properties, $\boldsymbol{\theta}$, are unaffected by changes in the microstructure morphology, such that the identified posterior distribution $p(\boldsymbol{\theta} \mid \boldsymbol{\sigma}^E, \varepsilon_f^E, \boldsymbol{\alpha}^E)$ can be applied to new microstructures. In order to perform the operation specified in Eq. (22), a forward model predicting discretized stress values alongside a failure strain, defined as $\boldsymbol{\sigma}^M$ and ε_f^M, with the subscript (M) denoting a model output, must be established. This surrogate model would output a distribution $p(\boldsymbol{\sigma}^M, \varepsilon_f^M \mid \boldsymbol{\theta}, \boldsymbol{\alpha})$, which might then be used in performing Bayesian inference to identify $p(\boldsymbol{\theta} \mid \boldsymbol{\sigma}^E, \varepsilon_f^E, \boldsymbol{\alpha}^E)$. Based on the description in Section 3.3, the prediction of $p(\boldsymbol{\sigma}^M, \varepsilon_f^M \mid \boldsymbol{\theta}, \boldsymbol{\alpha})$ is the result of a simple transformation of $p(\boldsymbol{\sigma}^M, \overline{\mathbf{Y}}_1^M \mid \boldsymbol{\theta}, \boldsymbol{\alpha})$ utilizing Y_{1C} as a stochastic model parameter. There are two major challenges to the practical implementation of Eq. (22). First, the training of the surrogate model $p(\boldsymbol{\sigma}^M, \varepsilon_f^M \mid \boldsymbol{\theta}, \boldsymbol{\alpha})$ would require a large dataset covering the exceedingly high-dimensional joint product space spanned by both $\boldsymbol{\alpha}$ and $\boldsymbol{\theta}$ (this includes the 12 CDM model parameters, the critical strain-energy release rate, Y_{1C}, and all principal components of the tow auto-correlations considered in the model building), demanding excessive or even prohibitive computational resources. Second, a sufficient number of μCT experimental scans would be necessary to have confidence that the distribution $p(\boldsymbol{\alpha}^E)$ is adequately characterized. This is because significant variations are expected between microstructures at different locations even within an individual composite panel. Indeed, this can be seen in Fig. 4, where the two experimental microstructures from the same panel do not lie directly upon each other. Conceptually, it should be understood that these individual measurements (visualized in the low dimensional PC space shown in Fig. 4) essentially reflect sampling of the underlying microstructure represented by the distribution $p(\boldsymbol{\alpha}^E)$ [87]. In order to circumvent the challenges described above, Eq. (22) is reformulated as

$$p(\boldsymbol{\sigma}^M, \varepsilon_f^M \mid \boldsymbol{\alpha}, \boldsymbol{\sigma}^E, \varepsilon_f^E, \boldsymbol{\alpha}^E) = \int p(\boldsymbol{\sigma}^M, \varepsilon_f^M \mid \boldsymbol{\theta}, \boldsymbol{\alpha}) \left[\int p(\boldsymbol{\theta} \mid \boldsymbol{\sigma}^E, \varepsilon_f^E, \tilde{\boldsymbol{\alpha}}) p(\tilde{\boldsymbol{\alpha}} \mid \boldsymbol{\alpha}^E) d\tilde{\boldsymbol{\alpha}} \right] d\boldsymbol{\theta} \tag{23}$$

to permit a more practical computational strategy. The main steps of the proposed protocol entail:

1. Estimate the experimental microstructure conditional distribution $p(\tilde{\boldsymbol{\alpha}} \mid \boldsymbol{\alpha}^E)$, where $\tilde{\boldsymbol{\alpha}}$ represents the elusive underlying microstructure in the experiments (represented by a vector of its PC scores). This is accomplished through suitable sampling of the digitally generated microstructure ensemble for this study. Produce reduced-order SV-MOGPs capturing $p(\boldsymbol{\sigma}^M, \varepsilon_f^M \mid \boldsymbol{\theta}, \tilde{\boldsymbol{\alpha}})$ using the approaches described in Section 2.4.
2. Compute the posterior distribution $p(\boldsymbol{\theta} \mid \boldsymbol{\sigma}^E, \varepsilon_f^E, \tilde{\boldsymbol{\alpha}})$ by Bayesian inference using the Affine-Invariant MCMC algorithm described in Section 2.2.1. Note that the use of surrogate models developed in Step 1 are critical for enabling this step.
3. Produce updated reduced-order SV-MOGPs $p(\boldsymbol{\sigma}^M, \varepsilon_f^M \mid \tilde{\boldsymbol{\theta}}, \boldsymbol{\alpha})$, where $\tilde{\boldsymbol{\theta}}$ represents the subspace of $\boldsymbol{\theta}$ supported by the posterior $p(\boldsymbol{\theta} \mid \boldsymbol{\sigma}^E, \varepsilon_f^E, \tilde{\boldsymbol{\alpha}})$ established in Step 2, and incorporated these updated surrogate models in computing the outer marginalization in Eq. (23).

A visual depiction of the protocol described above can be seen in Fig. 6. This protocol promises to address the multiple major challenges encountered in enabling probabilistic microstructure-sensitive predictions given sparse experimental data. These include (i) the consideration of the extremely high-dimensional product space of $\{\boldsymbol{\theta}, \boldsymbol{\alpha}\}$, (ii) the high cost of obtaining experimental microstructure information, and (iii) linking the stochastic treatment of constitutive model parameters across hierarchical microstructural length-scales. Most importantly, the protocol described above allows practical consideration of the extremely high-dimensional product space $\{\boldsymbol{\theta}, \boldsymbol{\alpha}\}$ through the incorporation of information contained in the limited, incomplete, and uncertain experimental data available. For the present problem, this was accomplished by first limiting the consideration of the microstructure subspace to a limited neighborhood near experimental observations, establishing the posterior for the model parameters, and then expanding the microstructure space to cover the full region of interest.

4. Results and discussion

4.1. Initial SV-MOGPs

As noted in the previous section, initial SV-MOGPs are needed to provide predictions of $p(\boldsymbol{\sigma}^M, \varepsilon_f^M \mid \boldsymbol{\theta}, \tilde{\boldsymbol{\alpha}})$, for which it is necessary to estimate the subset of microstructures characterizing the experimental microstructure conditional distribution $p(\tilde{\boldsymbol{\alpha}} \mid \boldsymbol{\alpha}^E)$. In the MKS framework, this is easily accomplished by identifying virtual microstructures exhibiting similar low-dimensional 2-point spatial correlations representations to the experimental microstructure scans. Note that the transformation through PCA preserves distance, involving solely a pure rotation, and any error in representation is introduced only in the truncation of the PC basis representing the data [123,124]. As the PC basis is optimized for the capture of variance, the truncation level can be set to ensure a minimal acceptable error in the estimated distances between the microstructures in the truncated low-dimensional PC space [123,124]. In this study, the distribution $p(\tilde{\boldsymbol{\alpha}} \mid \boldsymbol{\alpha}^E)$ was approximated by sampling the digitally generated microstructure ensemble (Section 3.2) and ranking according to the expression

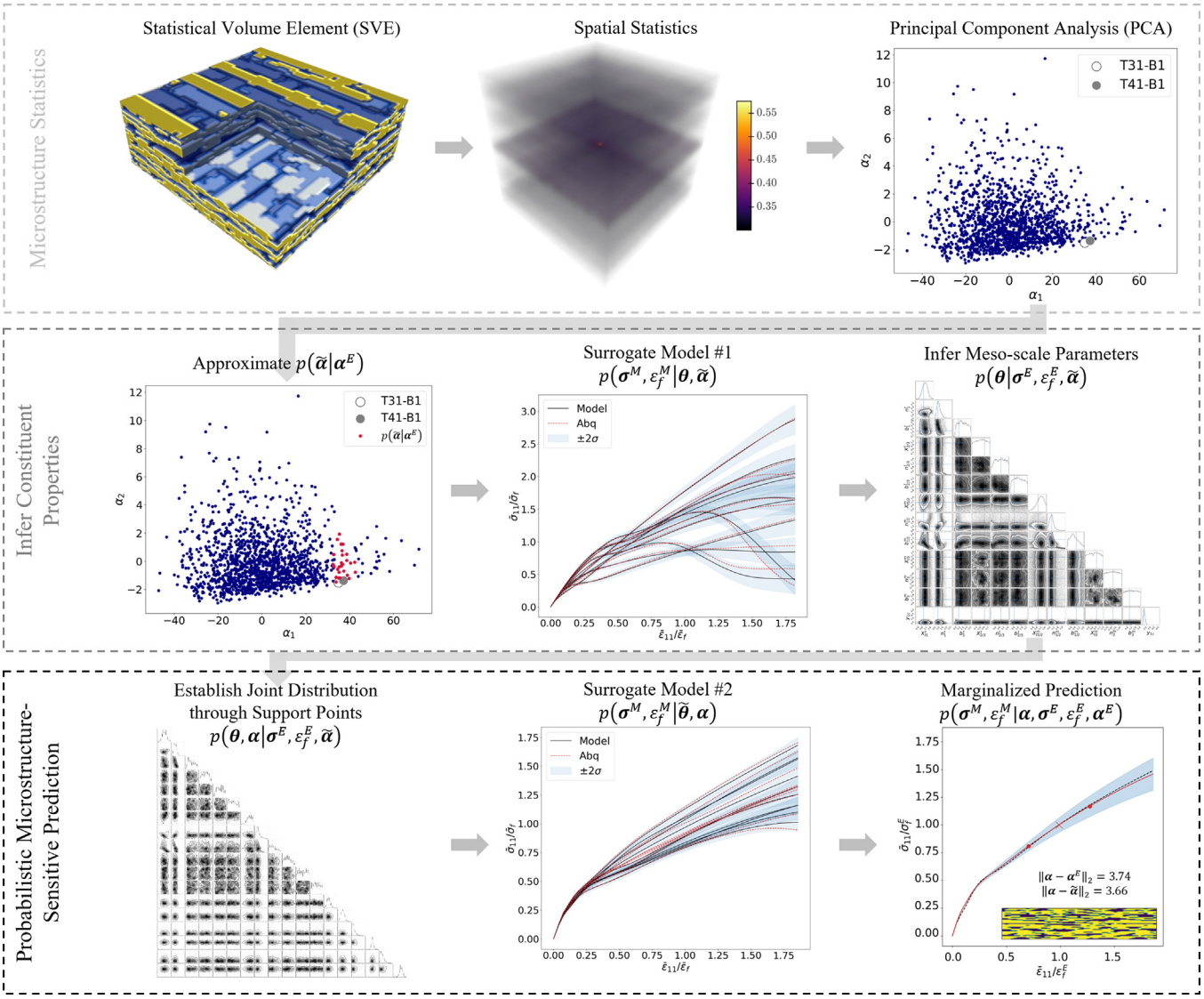

Fig. 6. Depiction detailing the main steps involved in the stochastic scale-bridging framework.

$\|\boldsymbol{\alpha}_i - \overline{\boldsymbol{\alpha}}^E\|_2$, where $\boldsymbol{\alpha}_i$ denotes the vector of PC scores for the digitally generated microstructure i, and $\overline{\boldsymbol{\alpha}}^E = \mathbb{E}[\boldsymbol{\alpha}^E]$ (i.e., $\overline{\boldsymbol{\alpha}}^E$ was identified as the mean of the spatial correlations of the two μCT experimental scans). Sampling was performed using a half-Gaussian distribution $\mathcal{HN}(0, 3.16)$, where the standard deviation was selected to represent the distance to the closest microstructure from the generated ensemble[3]. The subset of digitally generated microstructures exhibiting significant values of $p(\tilde{\boldsymbol{\alpha}} \mid \boldsymbol{\alpha}^E)$ were then combined with $\boldsymbol{\theta}$ values sampled with a Maximum Projection Latin hypercube design (MaxPro-LHD) [125,126] to identify the training and test datasets (total size of 2,000 Abaqus simulations) for building the initial SV-MOGP models in Step 1 of the protocol. MaxPro-LHD schemes provide for space-filling properties into lower dimensional projections, which are particularly advantageous in cases where only a few dimensions are expected to be active.

In order to provide predictions of $p(\boldsymbol{\sigma}^M, \varepsilon_f^M \mid \boldsymbol{\theta}, \tilde{\boldsymbol{\alpha}})$, SV-MOGPs were constructed for the stress array, $p(\boldsymbol{\sigma}^M \mid \boldsymbol{\theta}, \tilde{\boldsymbol{\alpha}})$ and the mean tow specific strain-energy release rate array, $p(\overline{\mathbf{Y}}_1^M \mid \boldsymbol{\theta}, \tilde{\boldsymbol{\alpha}})$, where the latter can provide predictions of the failure strain as $p(\varepsilon_f^M \mid \boldsymbol{\theta}, \tilde{\boldsymbol{\alpha}})$ through a transformation involving the critical longitudinal strain-energy release rate, Y_{1C}. Both SV-MOGP surrogate models were trained for 20,000 epochs with the RMSProp optimizer [127], utilizing a 80/20 train/test split, 40 latent GPs (L), 80 inducing points (Z), and cosine annealing of the learning rate. The predictive capabilities of these SV-MOGPs are illustrated in Fig. 6, with the model performance of $p(\boldsymbol{\sigma}^M \mid \boldsymbol{\theta}, \tilde{\boldsymbol{\alpha}})$ particularly highlighted. Predictions of the surrogate model $p(\overline{\mathbf{Y}}_1^M \mid \boldsymbol{\theta}, \tilde{\boldsymbol{\alpha}})$ are shown for exemplar sets of $\boldsymbol{\theta}$ in Fig. 7b. For each of the trained models, mean error metrics across the predicted arrays are shown inlaid in the respective Figs. 6a and 6b. Additional model error metrics are shown in Fig. 7c showing the NMAE calculated at each point in the predicted array for the model $p(\boldsymbol{\sigma}^M \mid \boldsymbol{\theta}, \tilde{\boldsymbol{\alpha}})$. Fig. 7c demonstrates the degradation in surrogate model predictions where an increasing number of sampled test points of $\boldsymbol{\theta}$ exhibit material softening.

4.2. CDM Model parameter posterior distribution

Equipped with both SV-MOGP surrogate models established in Section 4.1, a likelihood could be established for Bayesian inference defined in the second step of the proposed protocol as

[3] This process represents a method for implementing $\tilde{\boldsymbol{\alpha}}_i = \overline{\boldsymbol{\alpha}}^E + \boldsymbol{\xi}_i$ where $\|\boldsymbol{\xi}_i\|_2 \sim \mathcal{HN}(0, 3.16)$ in a setting with discrete options for $\tilde{\boldsymbol{\alpha}}_i$.

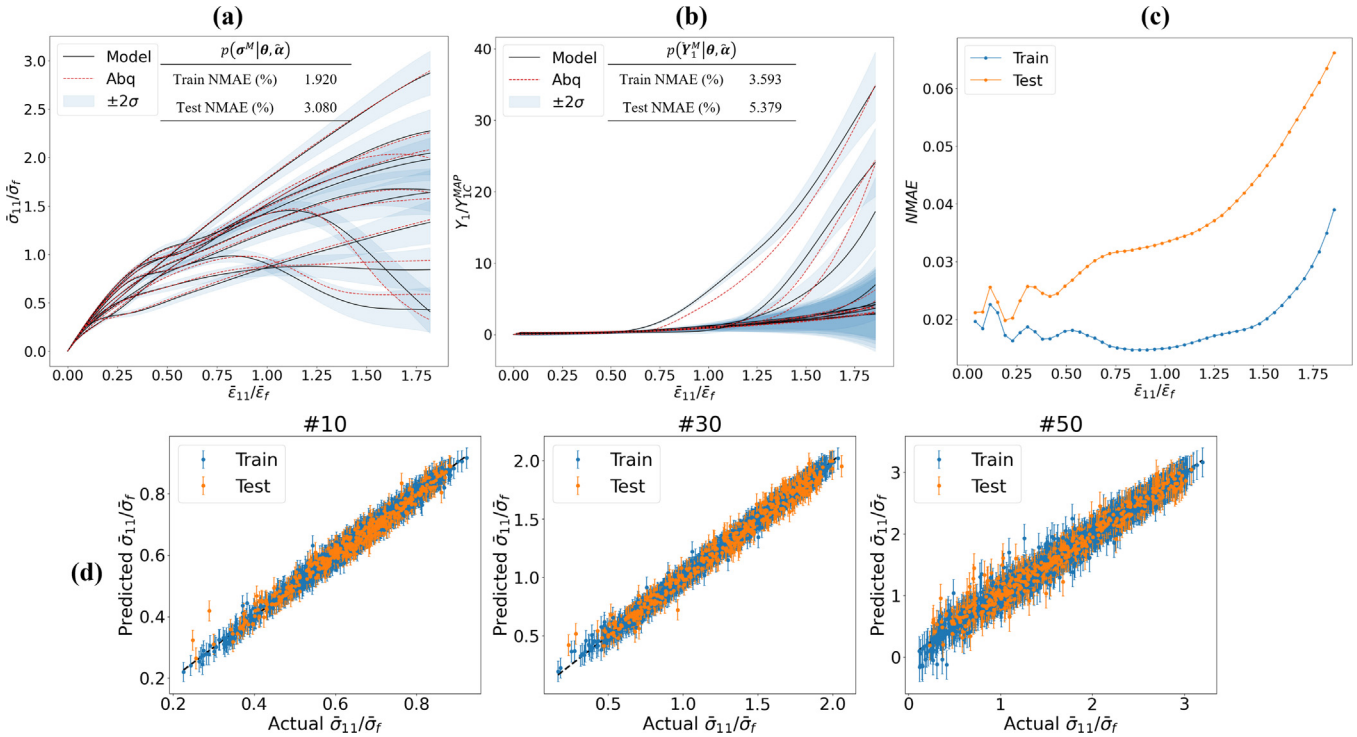

Fig. 7. Performance of SV-MOGPs for the prediction of tensile stress–strain curves and strain energy release rate. (a) Probabilistic prediction with $p(\boldsymbol{\sigma}^M \mid \boldsymbol{\theta}, \tilde{\boldsymbol{\alpha}})$ conditioned upon 10 sets of $\boldsymbol{\theta}$ from the test set along with mean error metrics of mean prediction for both training and test sets. (b) Probabilistic prediction with $p(\overline{\mathbf{Y}}_1^M \mid \boldsymbol{\theta}, \tilde{\boldsymbol{\alpha}})$ conditioned upon 10 sets of $\boldsymbol{\theta}$ from the test set along with mean error metrics of mean prediction for both training and test sets. (c) NMAE for $p(\boldsymbol{\sigma}^M \mid \boldsymbol{\theta}, \tilde{\boldsymbol{\alpha}})$ corresponding to the strain array values used in this study. (d) Parity plots at three selected values along the predicted stress–strain curves. Prediction of $\pm 2.0\sigma$ confidence intervals are displayed in these parity plots.

$$p(\boldsymbol{\sigma}^E, \varepsilon_f^E \mid \boldsymbol{\theta}, \tilde{\boldsymbol{\alpha}}) = \frac{1}{(2\pi)^{(N+1)/2}\sqrt{|\mathbf{K}|}} \exp\left[-\frac{1}{2}\left(\mathbb{E}\begin{bmatrix}\boldsymbol{\sigma}^E \\ \varepsilon_f^E\end{bmatrix} - \begin{bmatrix}\boldsymbol{\sigma}^M \\ \varepsilon_f^M\end{bmatrix}\right)^{\top} \times \mathbf{K}^{-1}\left(\mathbb{E}\begin{bmatrix}\boldsymbol{\sigma}^E \\ \varepsilon_f^E\end{bmatrix} - \begin{bmatrix}\boldsymbol{\sigma}^M \\ \varepsilon_f^M\end{bmatrix}\right)\right] \tag{24}$$

where $\mathbf{K} = \mathrm{diag}(\boldsymbol{\Sigma}^E + \boldsymbol{\Sigma}^M)$, with $\boldsymbol{\Sigma}^E$ denoting the covariance matrix directly computed from experimental observations, and $\boldsymbol{\Sigma}^M$ the constructed covariance matrix utilizing the posterior predictive distribution of both SV-MOGP surrogate models. The main diagonal of the covariance matrices is considered in isolation due to the assumption of uncorrelated heteroscedastic noise in the experimental measurements. This likelihood naturally arises from the governing statistical model defined in Eq. (7) considering Gaussian noise. Importantly, the selection of SV-MOGPs as the surrogate models in this work is particularly advantageous as $\mathcal{GP}$s provide prediction uncertainty estimates which can be incorporated into the likelihood covariance structure [77,76]. Utilizing the notation introduced in the above discussion, Bayes' theorem could be expressed for this application as

$$p(\boldsymbol{\theta} \mid \boldsymbol{\sigma}^E, \varepsilon_f^E, \tilde{\boldsymbol{\alpha}}) = \frac{p(\boldsymbol{\sigma}^E, \varepsilon_f^E \mid \boldsymbol{\theta}, \tilde{\boldsymbol{\alpha}}) p(\boldsymbol{\theta})}{\int p(\boldsymbol{\sigma}^E, \varepsilon_f^E \mid \boldsymbol{\theta}, \tilde{\boldsymbol{\alpha}}) p(\boldsymbol{\theta}) d\boldsymbol{\theta}} \tag{25}$$

A combination of uninformative uniform prior distributions alongside informative Gaussian distributions were incorporated into $p(\boldsymbol{\theta})$. These univariate priors are summarized in Table 2, where distributions for initial strengths $\{X_{t1}^t, X_{t2/3}^t, X_{t1/2}^m, X_{t3}^m\}$ were informed by the works of Almansour [128], Jacques et al. [129], Morcher et al. [9], and Bansal and Lamon [7].

The Affine-Invariant MCMC algorithm was used to establish the posterior distribution of the complete set of CDM model parameters. The posterior was estimated using 200 walkers and sampling for 400,000 iterations with an acceptance rate of 15%. The walkers were initialized randomly within support of the prior distribution and the likelihood function evaluated through repeated calls of the two SV-MOGP surrogate models. Convergence of MCMC sampling was evaluated through stabilization of the mean of all chains evaluated through trace plots and the mean estimated integrated autocorrelation time (final value of 4,600 across all dimensions sampled). 100,000 iterations were removed as burn-in and the remainder of the chains kept as the final result. Trace plots can be seen in Fig. 8a demonstrating stabilization of the mean across all chains. The sampled 200 chains were thinned by a factor of half the mean estimated integrated autocorrelation time and stacked, where the resulting posterior distribution can be visualized in a scatter plot matrix in Fig. 8b. The marginal distributions on the main diagonal intuitively display the degree of certainty regarding each damage parameter, while the off-diagonal displays projections of the posterior.

From closer inspection, parameters which heavily influence behavior of the SVE in the main loading direction such as $\{X_{t1}^t, n_1^t, b_1^t, X_{t1/2}^m, n_{1/2}^m, b_{1/2}^m\}$ (i.e., parameters controlling in-plane effective matrix behavior and tow on axis behavior) are more readily identified while others, such as matrix out-of-plane properties $\{X_{t3}^m, n_3^m, b_3^m\}$ are poorly identified as loading in-plane provides little information to reduce uncertainty on these parameters. Summary statistics of the posterior estimate are provided in Table 3.

The posterior distribution was then sampled, passed through the two forward models (SV-MOGP surrogate models), and

Table 2
Prior distributions applied to the 13-dimensional damage model parameter vector. Superscripts denote tows (t) or matrix (m) and the subscripts identify the principal material axes to which the parameter is applied. $\mathcal{U}$ denotes the uniform distribution, and $X_{t\alpha}^{t/m}$ values are in MPa.

$\boldsymbol{\theta}$	$p(\boldsymbol{\theta})$
X_{t1}^{t}	$\mathcal{N}(350, 100)$
n_{t1}^{t}	$\mathcal{U}(0.01, 0.3)$
b_{t1}^{t}	$\mathcal{U}(1, 50)$
$X_{t2/3}^{t}$	$\mathcal{N}(50, 50)$
$n_{t2/3}^{t}$	$\mathcal{U}(0.01, 5.0)$
$b_{t2/3}^{t}$	$\mathcal{U}(0.01, 100)$
X_{t1}^{m}	$\mathcal{N}(50, 50)$
n_{t1}^{m}	$\mathcal{U}(0.01, 0.8)$
b_{t1}^{m}	$\mathcal{U}(0.01, 2.0)$
$X_{t2/3}^{m}$	$\mathcal{N}(15, 15)$
$n_{t2/3}^{m}$	$\mathcal{U}(1, 2)$
$b_{t2/3}^{m}$	$\mathcal{U}(0.1, 30)$
Y_{1C}	$\mathcal{U}(0, 40)$

Table 3
Statistical measures of marginalized posterior distributions including the mean, standard deviation, skewness, and kurtosis. All values are normalized by the corresponding MAP value for each parameter.

$\boldsymbol{\theta}$	Mean	Std. Dev.	Skew.	Kurt.
X_{t1}^{t}	1.159	0.259	0.109	−0.042
n_{t1}^{t}	1.086	0.255	0.877	0.985
b_{t1}^{t}	1.544	0.600	0.089	−1.091
$X_{t2/3}^{t}$	0.718	0.397	−0.018	−1.155
$n_{t2/3}^{t}$	0.927	0.474	−0.018	−1.125
$b_{t2/3}^{t}$	1.894	0.933	0.078	−1.122
X_{t1}^{m}	1.175	0.396	−0.612	−0.107
n_{t1}^{m}	1.068	0.456	1.751	3.920
b_{t1}^{m}	0.809	0.403	0.309	−0.781
$X_{t2/3}^{m}$	0.787	0.422	−0.027	−1.172
$n_{t2/3}^{m}$	0.987	0.187	0.018	−1.180
$b_{t2/3}^{m}$	1.360	0.760	−0.015	−1.196
Y_{1C}	1.138	0.358	1.238	8.632

displayed against the experimental stress–strain curves in Fig. 9. A total 10,000 samples were used in Fig. 9a. The distribution of the strain to failure (Fig. 9b) reflects the assumed Gaussian distribution of the experimental results.

4.3. Microstructure-sensitive probabilistic prediction

The third step in the three-step Bayesian calibration procedure involves refining the domain of $\boldsymbol{\theta}$ to the subspace $\tilde{\boldsymbol{\theta}}$, informed through the posterior identified in the second step, $p(\boldsymbol{\theta} \mid \boldsymbol{\sigma}^E, \varepsilon_f^E, \tilde{\boldsymbol{\alpha}})$, and displayed in Fig. 8b. This information is then utilized to produce the previously intractable final grouping of surrogate models for the prediction of $p(\boldsymbol{\sigma}^M, \varepsilon_f^M \mid \boldsymbol{\alpha}, \boldsymbol{\sigma}^E, \varepsilon_f^E, \tilde{\boldsymbol{\alpha}}, \tilde{\boldsymbol{\theta}})$.

The mechanics of forming the training data for these models consists of establishing the desired joint distribution $p(\boldsymbol{\theta}, \boldsymbol{\alpha} \mid \boldsymbol{\sigma}^E, \varepsilon_f^E, \tilde{\boldsymbol{\alpha}})$ through the previously sampled points defining

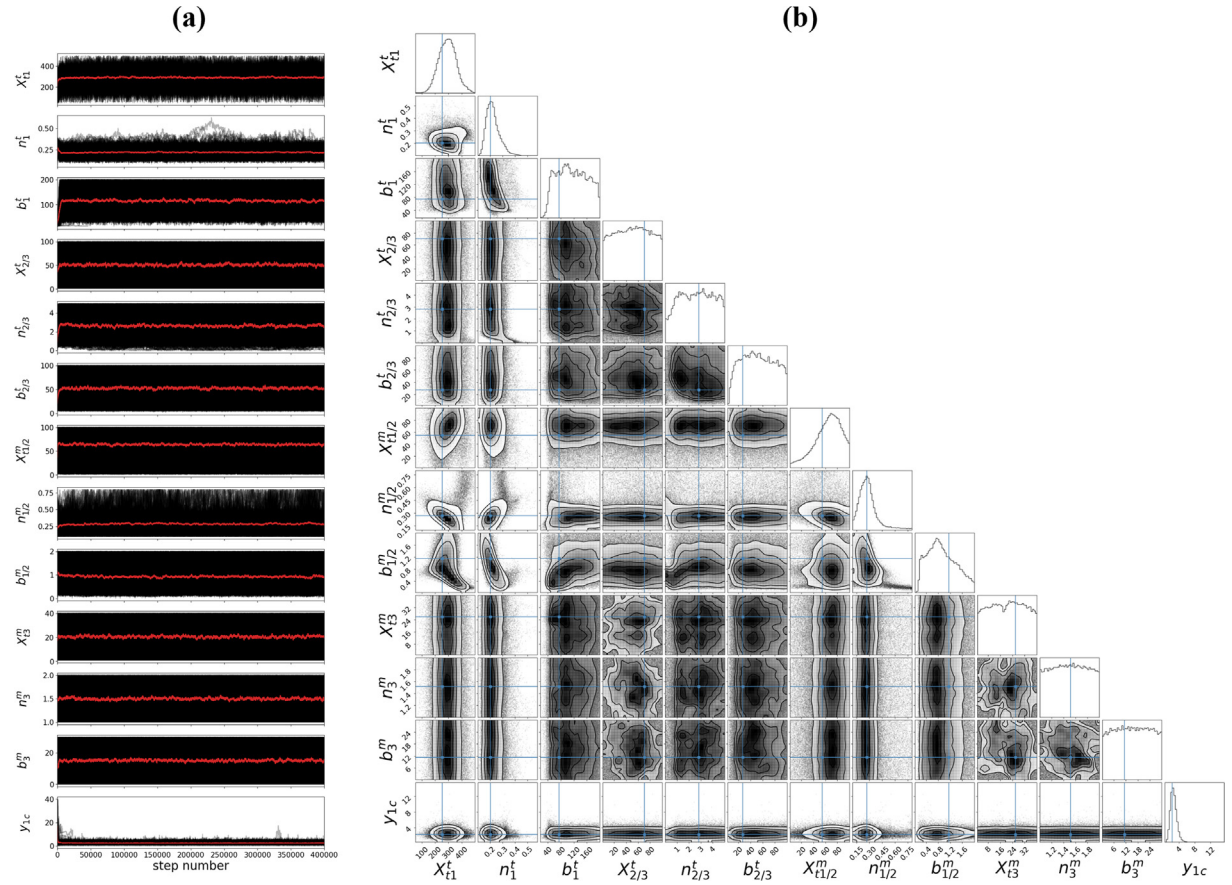

Fig. 8. Inferred 13-dimensional posterior distribution estimate of CDM model parameters of microstructure constituents. (a) Trace plots from MCMC sampling of all walkers demonstrating convergence of the mean in red. (b) Scatter plot matrix of the posterior distribution, with the maximum a posteriori (MAP) value highlighted in blue. All parameters are normalized by their respective MAP value. Contours denote the 0.5σ, 1.0σ, 1.5σ, and 2.0σ confidence intervals. Plotting was performed with a Python package by Foreman-Mackey [130].

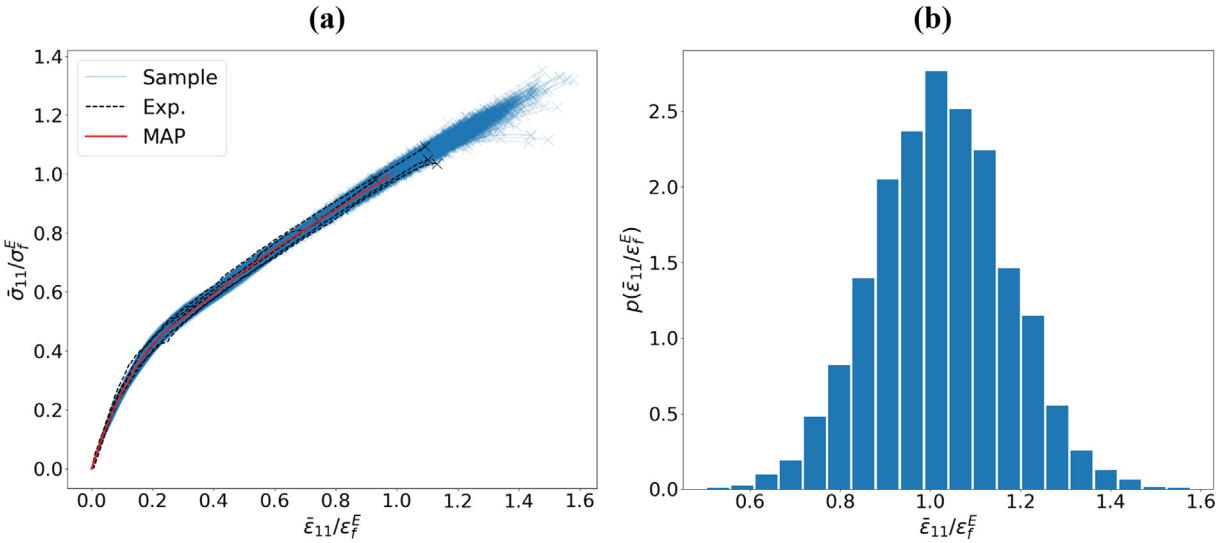

Fig. 9. Forward propagation of 10,000 samples from the posterior distribution through both SV-MOGP surrogate models. (a) The sampled stress–strain curves are plotted in blue, along with the curve resulting from the MAP vector in red and the experimentally observed response in black. (b) Histogram of strain to failure obtained from the propagation of sampled values of Y_{1C}.

the posterior of model parameters, and the individual points in the principal component space defining the microstructure ensemble. In order to form this distribution, compaction of the constituent damage parameter posterior, consisting of 46,200 unique samples was performed through the use of support points (described in Section 2.2.2), resulting in 1,500 support points summarizing the distribution. With equivalent numbers of points characterizing both the distributions $p(\boldsymbol{\theta} \mid \boldsymbol{\sigma}^E, \varepsilon_f^E, \tilde{\boldsymbol{\alpha}})$ and $p(\boldsymbol{\alpha})$, an outer product could be performed to generate an estimate of $p(\boldsymbol{\theta}, \boldsymbol{\alpha} \mid \boldsymbol{\sigma}^E, \varepsilon_f^E, \tilde{\boldsymbol{\alpha}})$. The identification of support points was performed once more to reduce the dimensionality of the joint distribution, $p(\boldsymbol{\theta}, \boldsymbol{\alpha} \mid \boldsymbol{\sigma}^E, \varepsilon_f^E, \tilde{\boldsymbol{\alpha}})$ from 2,250,000 points to 2,000. This process is illustrated in Fig. 10, where Fig. 10a displays a scatter plot matrix

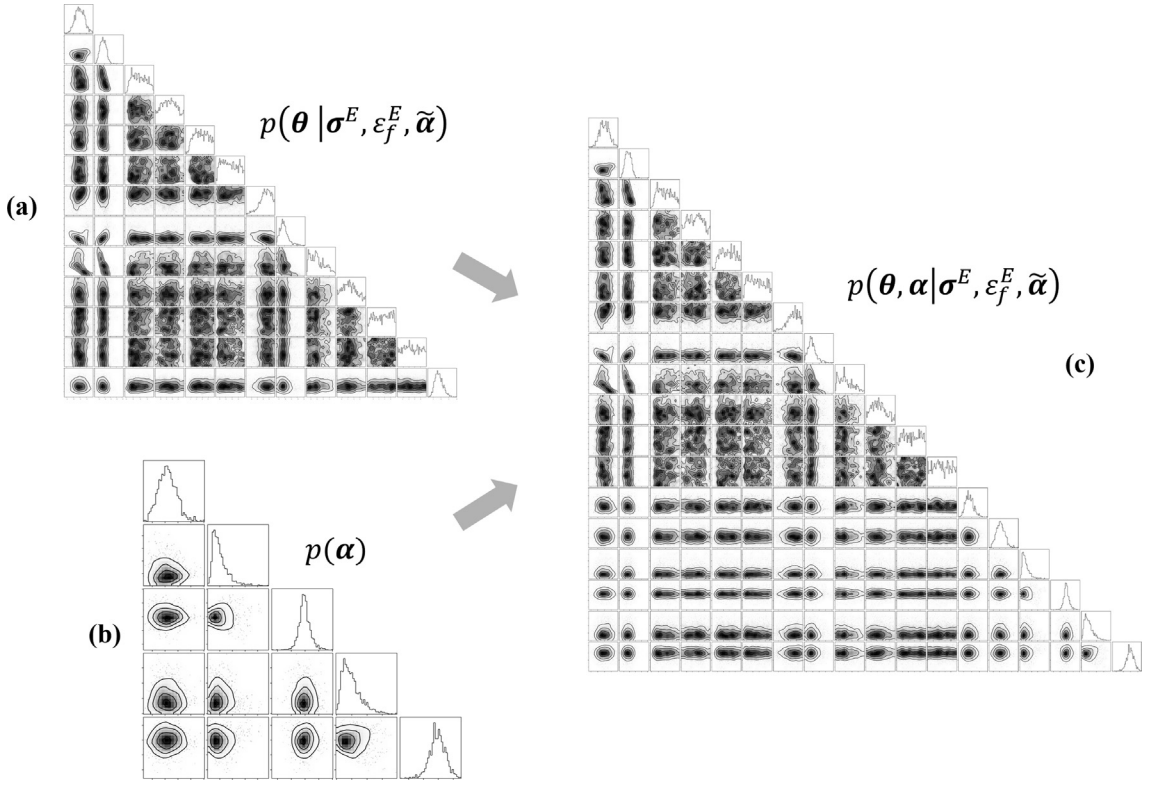

Fig. 10. Illustration of establishing an estimate of the joint distribution $p(\boldsymbol{\theta}, \boldsymbol{\alpha} \mid \boldsymbol{\sigma}^E, \varepsilon_f^E, \tilde{\boldsymbol{\alpha}})$. (a) Compact representation of posterior of CDM model parameters through the use of support points. (b) distribution of principal components of 2-point spatial correlations of microstructure ensemble (restricted to 5 principal components for visual clarity). (c) Compact representation of joint distribution of microstructure and posterior of CDM model parameters.

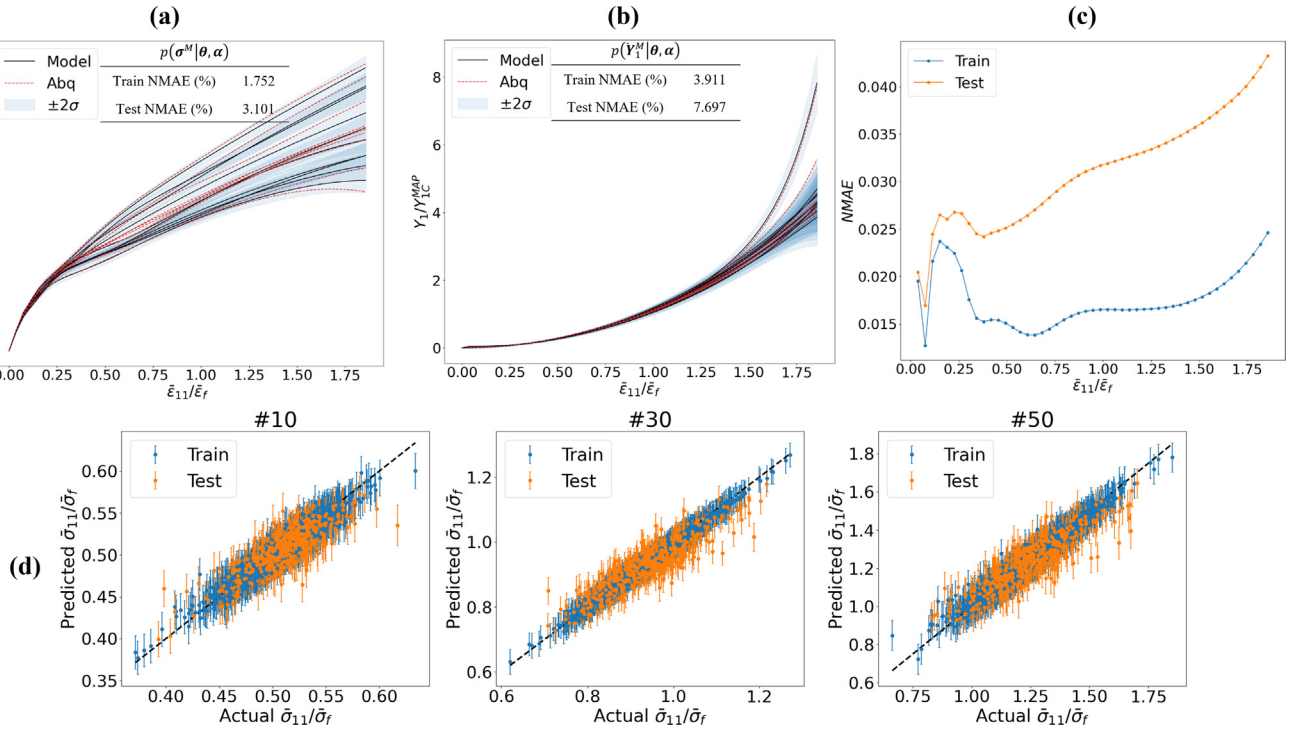

Fig. 11. Performance of the final SV-MOGPs built for the prediction of tensile stress–strain curves and strain energy release rate. (a) Probabilistic prediction with $p(\boldsymbol{\sigma}^M \mid \boldsymbol{\theta}, \boldsymbol{\alpha})$ conditioned upon 10 sets of $\{\boldsymbol{\theta}, \boldsymbol{\alpha}\}$ from the test set along with mean error metrics of mean prediction for both training and test sets. (b) Probabilistic prediction with $p(\overline{\mathbf{Y}}_1^M \mid \boldsymbol{\theta}, \boldsymbol{\alpha})$ conditioned upon 10 sets of $\{\boldsymbol{\theta}, \boldsymbol{\alpha}\}$ from the test set along with mean error metrics of mean prediction for both training and test sets. (c) NMAE for $p(\boldsymbol{\sigma}^M \mid \boldsymbol{\theta}, \boldsymbol{\alpha})$ corresponding to the strain array values used in this study. (d) Parity plots at three selected values along the predicted stress–strain curves. Prediction of $\pm 2.0\sigma$ confidence intervals are displayed in these parity plots.

of the compact representation of the CDM model parameter posterior shown in Fig. 8b, and Fig. 10c displays the compact result of the product of the two independent distributions providing the desired joint $p(\boldsymbol{\theta}, \boldsymbol{\alpha} \mid \boldsymbol{\sigma}^E, \varepsilon_f^E, \tilde{\boldsymbol{\alpha}})$.

The 2,000 support points constituting the multi-dimensional joint distribution in Fig. 10c could then finally be treated as individual training data points for which Abaqus input files could be generated. In a similar fashion to the first step of this Bayesian workflow, the result of the FE-simulations provided training data encompassing both homogenized stress–strain curves alongside evolution of the strain energy release rate for tows predominantly oriented in the direction of loading. These final two SV-MOGP surrogate models were also trained for 20,000 epochs with the RMSProp optimizer [127] utilizing a 80/20 train/test split, 40 latent GPs (L), and 80 inducing points (Z). The predictive accuracy of these models is depicted in Fig. 11. The input vector for these models comprised the 12 initial CDM model parameters (with Y_{1C} excluded as it contains no predictive information for either model), and the first 10 principal components of the 2-point spatial correlations.

The SV-MOGPs could then be used to evaluate the right-hand side of Eq. (23) for a given microstructure, utilizing the support points which capture the posterior distribution of CDM model parameters, $p(\boldsymbol{\theta} \mid \boldsymbol{\sigma}^E, \varepsilon_f^E, \tilde{\boldsymbol{\alpha}})$. This process provides the desired probabilistic prediction of tensile stress–strain response and failure strain, conditioned on the limited available experimental data. Example predictions for microstructures selected from the digitally created ensemble of microstructures are shown in Fig. 12. The distance of all microstructures selected from $\tilde{\boldsymbol{\alpha}}$ and $\boldsymbol{\alpha}^E$ is shown inlaid directly above each microstructure cross-section, where in particular, microstructure #645 demonstrates markedly similar 2-point spatial correlations to the experimentally observed μCT scans. This similarity through minimal distance in principal component space of the 2-point spatial correlations can also be observed in Fig. 4.

For each of the sampled microstructures from the ensemble it can be observed that the predicted distributions encompass the evaluated FE-simulated results, where the FE-simulation results displayed are for a single instantiation of the CDM model parameter vector from the posterior identified in Task 2 of the Bayesian workflow. Uncertainty in the CDM model parameters as inferred from the initial macroscale uniaxial stress–strain curves, and the effect of this uncertainty on constituent damage evolution is readily apparent in the increasing $\pm 2.0\sigma$ bounds during progressive loading of all microstructures. It is rather interesting to note that these prediction uncertainty bounds are not strongly correlated with similarity to the expected value of either $\tilde{\boldsymbol{\alpha}}$, or $\boldsymbol{\alpha}^E$ [4]. While microstructures such as #952 are clearly markedly different to $\tilde{\boldsymbol{\alpha}}$, demonstrating increasing uncertainty in response, others such as #27 are similarly different from $\tilde{\boldsymbol{\alpha}}$ while providing predictions with similar uncertainty to #645. This behavior demonstrates the ability of the second grouping of SV-MOGPs to learn the complex relationship mapping the joint space of $\{\boldsymbol{\theta}, \boldsymbol{\alpha}\}$ to the corresponding uniaxial tensile response, and the ability to utilize this gained knowledge in marginalizing out the identified posterior $p(\boldsymbol{\theta} \mid \boldsymbol{\sigma}^E, \varepsilon_f^E, \tilde{\boldsymbol{\alpha}})$ in making final microstructure-sensitive predictions.

[4] Denotation of expectation in distance metrics of selected microstructures to $\mathbb{E}[\boldsymbol{\alpha}^E]$ and $\mathbb{E}[\tilde{\boldsymbol{\alpha}}]$ in Fig. 12 has been omitted for notational clarity.

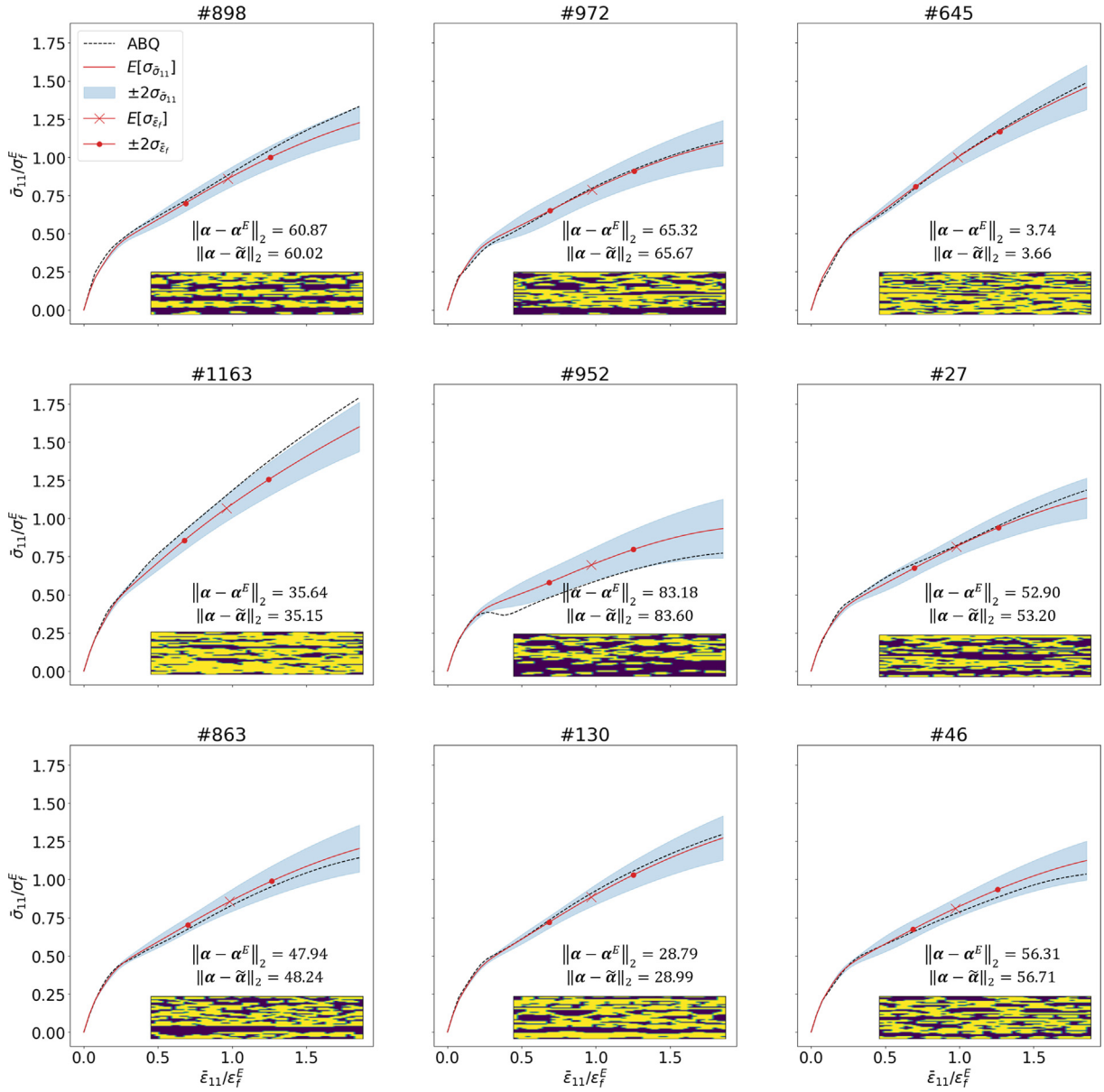

Fig. 12. Microstructure-sensitive probabilistic prediction of stress–strain curves for the 3 identified microstructures in Fig. 4, shown in the top row, alongside 6 randomly sampled microstructures. $X-Z$ cross-sections of evaluated microstructures are shown in-laid with prediction alongside distance in principal component space to $\tilde{\boldsymbol{\alpha}}$ and $\boldsymbol{\alpha}^E$. The mean stress–strain prediction is shown in red, with $\pm 2.0\sigma$ bounds shown in blue and the mean failure strain prediction is denoted by a cross, with $\pm 2.0\sigma$ bounds by dots. The FE-simulated response for a singular instantiation of $\boldsymbol{\theta}$ from the identified parameter posterior distribution is shown in a dashed black line.

5. Conclusions

A stochastic scale-bridging framework has been presented and demonstrated for the robust formulation of high-fidelity probabilistic surrogate models for the microstructure-sensitive prediction of effective stress–strain curves in woven composite architectures. Importantly, this framework presented several key ideas and practical simplifications enabling the propagation of uncertainty in macroscale experimental data, to mesoscale constituent damage evolution, and finally incorporating this information in low-cost macroscale microstructure-sensitive predictions of uniaxial tensile response. Chief of which includes an assumption of independence between constitutive model parameters and microstructure for a limited microstructural class. This assumption enabled the decomposition of the coupled stochastic inverse problem into one which could be approached in a sequential manner independently. The first portion of the proposed framework revolves around approximating the experimental microstructure generative function in the space of 2-point spatial correlations. Samples of this approximation enable the production of a surrogate model, as the microstructural domain is significantly constrained while there still exists significant uncertainty over the constitutive model parameters. Secondly, this surrogate model is then leveraged to infer a posterior of model parameters conditioned upon the observed macroscale experimental data. Lastly, this posterior of constitutive model parameters is then used to produce a second surrogate model covering a domain of constitutive model parameters constrained to the previously identified posterior, with microstructures sampled from the wider available ensemble.

At a higher level, the main contributions of this work are twofold. Firstly, the framework enables the statistical calibration of

constitutive model parameters at lower length-scales than the observed experimental data while accounting for experimental microstructure uncertainty. This is practically relevant as often experimental measurement techniques at lower length-scales are either non-existent, or exhibit impracticable large amounts of scatter. While this portion of the work was solely demonstrated for a single dataset consisting of uniaxial tensile stress–strain curves, the framework naturally allows for expansion to heterogeneous experimental datasets. One might imagine such datasets may lead to a sharpening of the posterior distribution, reflecting increased knowledge over such parameters. Secondly, the framework provided for a manner in propagating this inferred distribution at a lower-length scale towards higher length-scale probabilistic predictions of alternate microstructures. The prior assumption of independence between the identified posterior distribution and microstructure presents a limitation at this juncture. Through providing predictions by marginalization, an implicit assumption is made in which the constituent spatial arrangement of new microstructures for which predictions are sought, is sufficiently similar to the experimental microstructure, such that the local material response does not differ significantly from the observed experiments. This requires that the second portion of this framework be applied to microstructure ensembles in a narrow material class, while the first portion is sufficiently general.

As a whole, the presented framework permits the transformation of an initially intractable problem, namely, the development of a surrogate model jointly covering both the microstructure and constitutive model parameters input spaces, into one which is feasible computationally. Importantly, this work significantly weakens prior assumptions often present in hierarchical modeling through providing a method for stochastic bi-directional information flow across length-scales rather than deterministic assignment of material properties at the lowest length-scale considered in the hierarchy.

Data availability

The authors do not have permission to share data.

Declaration of Competing Interest

The authors declare that they have no known competing financial interests or personal relationships that could have appeared to influence the work reported in this paper.

Acknowledgements

This research was sponsored by Pratt & Whitney. This work utilized computing resources and services provided by the Partnership for an Advanced Computing Environment (PACE) and the Hive computing cluster at the Georgia Institute of Technology, Atlanta, Georgia, USA.

Appendix A

Further details regarding the surrogate model architecture utilized in this work can be found in this section. Utilizing the same notation presented in Section 2.4, the finite dimensional $\mathcal{GP}$ is distributed as

$$p(\mathbf{y} \mid \mathbf{X}, \boldsymbol{\theta}_k) = \mathcal{N}(\mathbf{0}, \mathbf{K_{ff}} + \sigma_y^2 \mathbf{I}),\ [\mathbf{K_{ff}}]_{nn'} = k(\mathbf{x}_n, \mathbf{x}'_n). \tag{A.1}$$

As mentioned previously, $\mathcal{GP}$ regression with small dimensional datasets provides a robust method of learning latent functions. The limitation in scalability presents itself with the computation of the inverse covariance matrix, $\left[\mathbf{K_{ff}} + \sigma_y^2 \mathbf{I}\right]^{-1}$, scaling as $\mathcal{O}(N^3)$ time and limiting its practicality when confronted with large datasets. Sparse approximations to this Gaussian process primarily rely upon developing methods of approximating this covariance matrix through the use of inducing points, or pseudo-inputs, enabling cost $\mathcal{O}(NM^2)$. Methods of this include the Deterministic Training Conditional (DTC) [131], the Fully Independent Training Conditional (FITC) [132], and the Variational Free Energy [93] approximations. Differences between these methods depend upon where the sparse assumption is made, where DTC and FITC make simplifying assumptions regarding dependencies in the training data, leading to an approximate generative model (through modifying the prior and space of functions considered), with the benefit of being able to perform exact inference. Detrimentally, this approach does not provide any distance metric between the exact non-sparse model and the final generated model, and the learning of inducing input locations through the likelihood can perform poorly (e.g. DTC is prone to overfitting even when $M \ll N$ [133]). The more elegant VFE incorporated in this work, pushes the approximation towards the time of inference and enables computation of the exact model. As mentioned in Section 2.4, the covariance function hyperparameters and inducing inputs are jointly optimized by maximizing a lower bound to the exact marginal likelihood, where the inducing input locations are considered to be variational parameters selected through minimization of the KL-divergence between the variational $\mathcal{GP}$ and the true posterior $\mathcal{GP}$. This lower bound to the exact marginal likelihood can be expressed using a distribution $q(f)$ over the entire infinite dimensional function as

$$\begin{aligned} \log p(\mathbf{y} \mid \boldsymbol{\theta}_k) &= \log \int p(\mathbf{y}, f \mid \boldsymbol{\theta}_k) df \qquad \geqslant \mathcal{F}(q, \boldsymbol{\theta}_k) \\ &= \int q(f) \log \tfrac{p(\mathbf{y}, f \mid \boldsymbol{\theta}_k)}{q(f)} df = \mathbb{E}_{q(f)}\left[\log \tfrac{p(\mathbf{y}, f \mid \boldsymbol{\theta}_k)}{q(f)}\right] \end{aligned} \tag{A.2}$$

where no limiting assumptions have been made regarding the form of $q(f)$. Alternatively, this VFE bound can be written as the difference between the model log-marginal likelihood and the KL divergence between the variational posterior and true posterior as

$$\mathcal{F}(q, \boldsymbol{\theta}_k) = \log p(\mathbf{y} \mid \boldsymbol{\theta}_k) - D_{KL}(q(f) \| p(f \mid \mathbf{y}, \boldsymbol{\theta}_k)) \tag{A.3}$$

where the bound is maximized when $q(f) = p(f \mid \mathbf{y}, \boldsymbol{\theta}_k)$. The reduction in computational complexity is achieved through the identification of a small set of $M \leqslant N$ inducing points $\mathbf{Z} = \{z_m\}_{m=1}^M$ which are independent of X, in order to provide a lower rank approximation to the full covariance $\mathbf{K_{ff}}$. The corresponding function values at these inducing points are then denoted as u. The disjoint infinite dimensional function can then be represented as $f = \{u, f_{\neq u}\}$, with an approximate posterior distribution of $q(f) = q(u, f_{\neq u} \mid \boldsymbol{\theta}_k) = p(f_{\neq u} \mid u, \boldsymbol{\theta}_k) q(u)$ (it should be highlighted, there is a slight abuse of notation using q to denote the variational distribution over both the infinite dimensional latent function and the finite dimension inducing values). Under this approximation, $f_{\neq u}$ is only influenced through the inducing points and not the data directly. This approximate posterior simplifies the VFE bound defined in Eq. (A.3) to that with only $O(NM^2)$ cost as

$$\begin{aligned} \mathcal{F}(q, \boldsymbol{\theta}_k) &= \mathbb{E}_{q(f \mid \theta)}\left[\log \tfrac{p(\mathbf{y} \mid f, \boldsymbol{\theta}_k) p(\mathbf{u} \mid \boldsymbol{\theta}_k)}{q(\mathbf{u})}\right] \\ &= \sum_{n=1}^{N} \mathbb{E}_{q(f \mid \theta)}[p(y_n \mid f_n, \boldsymbol{\theta}_k)] - D_{KL}(q(\mathbf{u}) \| p(\mathbf{u} \mid \boldsymbol{\theta}_k)). \end{aligned} \tag{A.4}$$

Maximization of this bound with respect to the variational posterior can be performed in closed form, with the optimal q^* unsurprisingly also being Gaussian and expressed as

$$\begin{aligned} q^*(f \mid \boldsymbol{\theta}_k) &= \operatorname*{argmax}_q \mathcal{F}(q, \boldsymbol{\theta}_k) \\ &= \mathcal{N}(f; \mathbf{Q}_{f\mathbf{f}} \widehat{\mathbf{K}}_{\mathbf{ff}}^{-1} \mathbf{y}, \mathbf{K}_{ff} - \mathbf{Q}_{f\mathbf{f}} \widehat{\mathbf{K}}_{\mathbf{ff}}^{-1} \mathbf{Q}_{\mathbf{f}f}) \end{aligned} \tag{A.5}$$

where $\hat{\mathbf{K}}_{\mathbf{ff}} = \mathbf{Q}_{\mathbf{ff}} + \sigma^2\mathbf{I}$, and $\mathbf{Q}_{\mathbf{ff}} = \mathbf{K}_{\mathbf{fu}}\mathbf{K}_{\mathbf{uu}}^{-1}\mathbf{K}_{\mathbf{uf}}$ provides the low rank approximation. For clarity, elements of the covariance matrices are calculated as $[\mathbf{K}_{\mathbf{uu}}]_{mm'} = k(\mathbf{z}_m, \mathbf{z}_{m'})$ and $[\mathbf{K}_{\mathbf{fu}}]_{nm'} = k(\mathbf{x}_m, \mathbf{z}_{m'})$. The optimal VFE bound utilizing the variational distribution identified in Eq. (A.5) is then

$$\mathcal{F}(q^*, \theta_k) = -\frac{N}{2}\log(2\pi) - \frac{1}{2}\log\left|\hat{\mathbf{K}}_{\mathbf{ff}}\right| - \frac{1}{2}\mathbf{y}^\top\hat{\mathbf{K}}_{\mathbf{ff}}^{-1}\mathbf{y} - \frac{1}{2\sigma_y^2}\mathrm{tr}(\mathbf{K}_{\mathbf{ff}} - \mathbf{Q}_{\mathbf{ff}}) \tag{A.6}$$

which can then be optimized with respect to the covariance function hyperparameters, θ_k. Importantly, this VFE bound contains a trace term which is missing from the DTC method discussed earlier, resulting in a penalty term preventing the known problems with overfitting present in the DTC method.

References

[1] Katoh Y, Ozawa K, Shih C, Nozawa T, Shinavski RJ, Hasegawa A, Snead LL. Continuous SiC fiber, CVI SiC matrix composites for nuclear applications: Properties and irradiation effects. J Nucl Mater 2014;448(1–3):448–76. https://doi.org/10.1016/j.jnucmat.2013.06.040. URL https://linkinghub.elsevier.com/retrieve/pii/S0022311513008647.

[2] DiCarlo JA. Advances in SiC/SiC composites for aero-propulsion, in: ceramic matrix composites. John Wiley & Sons Ltd; 2014, p. 217–235, section: 7 _eprint: https://onlinelibrary.wiley.com/doi/pdf/10.1002/9781118832998.ch7. https://doi.org/10.1002/9781118832998.ch7. https://onlinelibrary.wiley.com/doi/abs/10.1002/9781118832998.ch7.

[3] Aviation G. In aviation's material world, GE's CMCs unlock opportunity, library Catalog: blog.geaviation.com; Jul. 2018. URL https://blog.geaviation.com/product/in-aviations-material-world-ges-cmcs-unlock/.

[4] Snead LL, Nozawa T, Katoh Y, Byun T-S, Kondo S, Petti DA. Handbook of SiC properties for fuel performance modeling. J Nucl Mater 2007;371(1–3):329–77. https://doi.org/10.1016/j.jnucmat.2007.05.016. URL https://linkinghub.elsevier.com/retrieve/pii/S0022311507007623.

[5] Long A. Design and manufacture of textile composites. Woodhead Publishing Limited; 2005.

[6] Crookston JJ, Long AC, Jones IA. A summary review of mechanical properties prediction methods for textile reinforced polymer composites. Proc Inst Mech Eng, Part L: J Mater: Des Appl 2005;219(2):91–109. https://doi.org/10.1243/146442005X10319. URL http://journals.sagepub.com/doi/10.1243/146442005X10319.

[7] Bansal NP, Lamon J, editors. Ceramic matrix composites: materials, modeling and technology. Hoboken, NJ, USA: John Wiley & Sons Inc; 2014. https://doi.org/10.1002/9781118832998.

[8] Morscher G, Singh M, Kiser J, Freedman M, Bhatt R. Modeling stress-dependent matrix cracking and stress–strain behavior in 2D woven SiC fiber reinforced CVI SiC composites. Compos Sci Technol 2007;67(6):1009–17. https://doi.org/10.1016/j.compscitech.2006.06.007. URL https://linkinghub.elsevier.com/retrieve/pii/S0266353806002156.

[9] Morscher GN. Advanced Woven SiC/SiC composites for high temperature applications; Oct. 2007.

[10] Bansal NP. Handbook of ceramic composites, chemical vapor infiltrated SiC/SiC composites (CVI SiC/SiC). In: Handbook of ceramic composites, vol. 3, Kluwer Academic Publishers; 2005, p. 55–76.

[11] Jung J, Do BC, Yang QD. Augmented finite-element method for arbitrary cracking and crack interaction in solids under thermo-mechanical loadings. Philosoph Trans Roy Soc A: Mathe, Phys Eng Sci 2071;374: 2016: 20150282, publisher: Royal Society. https://doi.org/10.1098/rsta.2015.0282. https://royalsocietypublishing.org/doi/10.1098/rsta.2015.0282.

[12] Artz T, Yuan Z, Kumar R, Fish J. Computational model for oxidation-assisted rupture of ceramic matrix composites. Int J Solids Struct 2020;202:195–207. https://doi.org/10.1016/j.ijsolstr.2020.05.009. URL https://linkinghub.elsevier.com/retrieve/pii/S0020768320301761.

[13] Kumar RS, Mordasky M, Ojard G, Yuan Z, Fish J. Notch-strength prediction of ceramic matrix composites using multi-scale continuum damage model. Materialia 2019;6:100267. https://doi.org/10.1016/j.mtla.2019.100267. URL http://www.sciencedirect.com/science/article/pii/S2589152919300638.

[14] Pailhes J, Camus G, Lamon J. A constitutive model for the mechanical behavior of a 3D C/C composite. Mech Mater 2002;34(3):161–77. https://doi.org/10.1016/S0167-6636(01)00101-6. URL https://www.sciencedirect.com/science/article/pii/S0167663601001016.

[15] Hall RB, Brockman RA. Viscoelastoplastic oxidative multimode damage model for fibrous composite materials at extreme temperatures. In: Silberstein M, Amirkhizi A, editors. Challenges in mechanics of time dependent materials, vol. 2. Cham: Springer International Publishing; 2021. p. 55–8. https://doi.org/10.1007/978-3-030-59542-5_9.

[16] Hall RB, Brockman RA. Viscoelastoplastic damage with maximum rate of dissipation-based growth criterion and tri-component lie rate decomposition; Jun. 2019.

[17] Li J, Jiao G, Wang B, Li L, Yang C. Damage characteristics and constitutive modeling of the 2D C/SiC composite: Part II – Material model and numerical implementation. Chin J Aeronaut 2015;28(1):314–26. https://doi.org/10.1016/j.cja.2014.10.027. URL https://linkinghub.elsevier.com/retrieve/pii/S1000936114001812.

[18] Chaboche J, Lesné O, Pottier T.Continuum damage mechanics of composites: Towards a unified approach. In: Studies in Applied Mechanics, vol. 46, Elsevier; 1998, p. 3–26. https://doi.org/10.1016/S0922-5382(98)80032-9. https://linkinghub.elsevier.com/retrieve/pii/S0922538298800329.

[19] Oliver J. A consistent characteristic length for smeared cracking models. Int J Numer Meth Eng 1989;28(2):461–74. https://doi.org/10.1002/nme.1620280214. URL https://onlinelibrary.wiley.com/doi/10.1002/nme.1620280214.

[20] Matzenmiller A, Lubliner J, Taylor R. A constitutive model for anisotropic damage in fiber-composites. Mech Mater 1995;20(2):125–52. https://doi.org/10.1016/0167-6636(94)00053-0. URL https://linkinghub.elsevier.com/retrieve/pii/0167663694000530.

[21] Camus G. Modelling of the mechanical behavior and damage processes of fibrous ceramic matrix composites: application to a 2-D SiC/SiC. Int J Solids Struct 2000;37(6):919–42. https://doi.org/10.1016/S0020-7683(99)00065-7. URL https://www.sciencedirect.com/science/article/pii/S0020768399000657.

[22] Chaboche J-L, Maire J-F. A new micromechanics based CDM model and its application to CMC's. Aerosp Sci Technol 2002;6(2):131–45. https://doi.org/10.1016/S1270-9638(02)01154-9. URL https://linkinghub.elsevier.com/retrieve/pii/S1270963802011549.

[23] Van Oijen M, Rougier J, Smith R. Bayesian calibration of process-based forest models: bridging the gap between models and data. Tree Physiol 2005;25(7):915–27. https://doi.org/10.1093/treephys/25.7.915.

[24] Hill R. Elastic properties of reinforced solids: Some theoretical principles. J Mech Phys Solids 1963;11(5):357–72. https://doi.org/10.1016/0022-5096(63)90036-X. URL https://www.sciencedirect.com/science/article/pii/002250966390036X.

[25] McDowell DL, Ghosh S, Kalidindi SR. Representation and computational structure-property relations of random media. JOM 2011;63(3):45–51. https://doi.org/10.1007/s11837-011-0045-y. URL http://link.springer.com/10.1007/s11837-011-0045-y.

[26] Meyer P, Waas AM. FEM predictions of damage in continous fiber ceramic matrix composites under transverse tension using the crack band method. Acta Mater 2016;102:292–303. https://doi.org/10.1016/j.actamat.2015.09.002. URL https://www.sciencedirect.com/science/article/pii/S1359645415006680.

[27] Shan Z, Gokhale AM. Representative volume element for non-uniform microstructure. Comput Mater Sci 2002;24(3):361–79. https://doi.org/10.1016/S0927-0256(01)00257-9. URL https://www.sciencedirect.com/science/article/pii/S0927025601002579.

[28] Skinner T, Rai A, Chattopadhyay A. Multiscale ceramic matrix composite thermomechanical damage model with fracture mechanics and internal state variables. Compos Struct 2020;236:111847. https://doi.org/10.1016/j.compstruct.2019.111847. URL https://www.sciencedirect.com/science/article/pii/S0263822319338371.

[29] Zhang E, Chazot J, Antoni J. Parametric identification of elastic modulus of polymeric material in laminated glasses. IFAC Proc Vol 2012;45(16):422–7. https://doi.org/10.3182/20120711-3-BE-2027.00222. URL https://linkinghub.elsevier.com/retrieve/pii/S1474667015379878.

[30] El Moumen A, Kanit T, Imad A. Numerical evaluation of the representative volume element for random composites. Eur J Mech A. Solids 2021;86:104181. https://doi.org/10.1016/j.euromechsol.2020.104181. URL https://www.sciencedirect.com/science/article/pii/S099775382030560X.

[31] Przybyla CP, McDowell DL. Microstructure-sensitive extreme-value probabilities of high-cycle fatigue for surface vs. subsurface crack formation in duplex Ti–6Al–4V, Acta Mater 2012;60(1): 293–305. https://doi.org/10.1016/j.actamat.2011.09.031. https://www.sciencedirect.com/science/article/pii/S1359645411006689.

[32] Bishop CM. Pattern recognition and machine learning. Information science and statistics. New York: Springer; 2006.

[33] MacKay DJC. Information theory, inference, and learning algorithms. Cambridge University Press; 2003.

[34] Murphy KP. Machine learning: a probabilistic perspective. Adaptive computation and machine learning series. Cambridge, MA: MIT Press; 2012.

[35] Santner TJ, Williams BJ, Notz WI. The design and analysis of computer experiments. New York, NY: Springer Series in Statistics, Springer New York; 2018. https://doi.org/10.1007/978-1-4939-8847-1. URL http://link.springer.com/10.1007/978-1-4939-8847-1.

[36] Pacheo CC, Dulikravich GS, Vesenjak M, Borovinšek M, Duarte IMA, Jha R, et al. Inverse parameter identification in solid mechanics using Bayesian statistics, response surfaces and minimization. Technische Mechanik - Eur J Eng Mech 2016;36 (1–2):120–131, number: 1–2. https://doi.org/10.24352/UB.OVGU-2017-014. https://journals.ub.ovgu.de/index.php/techmech/article/view/695.

[37] Gallina A, Ambrozinski L, Pieczonka P, Uhl T, Staszewski W. Bayesian parameter identification of orthotropic composite materials using Lamb waves dispersion curves measurement - Alberto Gallina, Lukasz Ambrozinski, Pawel Packo, Lukasz Pieczonka, Tadeusz Uhl, Wieslaw J Staszewski. J Vib Control 23(16);2017. https://journals.sagepub.com/doi/full/10.1177/1077546315619264.

[38] Castillo A, Kalidindi SR. A Bayesian framework for the estimation of the single crystal elastic parameters from spherical indentation stress-strain

measurements. Front Mater 2019;6:136. https://doi.org/10.3389/fmats.2019.00136. URL https://www.frontiersin.org/article/10.3389/fmats.2019.00136/full.
[39] Fernandez-Zelaia P, Roshan Joseph V, Kalidindi SR, Melkote SN. Estimating mechanical properties from spherical indentation using Bayesian approaches. Mater Des 2018;147:92–105. https://doi.org/10.1016/j.matdes.2018.03.037. URL https://www.sciencedirect.com/science/article/pii/S0264127518302168.
[40] Mahnken R. Identification of material parameters for constitutive equations. In: Encyclopedia of computational mechanics. 2nd ed. American Cancer Society; 2017, p. 1–21, _eprint: https://onlinelibrary.wiley.com/doi/pdf/10.1002/9781119176817.ecm2043. https://doi.org/10.1002/9781119176817.ecm2043. https://onlinelibrary.wiley.com/doi/abs/10.1002/9781119176817.ecm2043.
[41] Zhang E, Chazot J, Antoni J, Hamdi M. Bayesian characterization of Young's modulus of viscoelastic materials in laminated structures. J Sound Vib 2013;332(16):3654–66. https://doi.org/10.1016/j.jsv.2013.02.032. URL https://linkinghub.elsevier.com/retrieve/pii/S0022460X13001879.
[42] Mehrez L, Kassem E, Masad E, Little D. Stochastic identification of linear-viscoelastic models of aged and unaged asphalt mixtures. J Mater Civil Eng 27 (4);2015. https://trid.trb.org/view/1317055.
[43] Miles P, Hays M, Smith R, Oates W. Bayesian uncertainty analysis of finite deformation viscoelasticity. Mech Mater 2015;91:35–49. https://doi.org/10.1016/j.mechmat.2015.07.002. URL https://www.sciencedirect.com/science/article/pii/S0167663615001490.
[44] Adeli E, Matthies HG. Parameter identification in viscoplasticity using transitional Markov Chain Monte Carlo Method, arXiv:1906.10647 [cs] ArXiv: 1906.10647. http://arxiv.org/abs/1906.10647.
[45] Adeli E, Rosic B, Matthies HG, Reinstädler S, Dinkler D. Comparison of Bayesian methods on parameter identification for a viscoplastic model with damage. Metals 2020;10(7):876. https://doi.org/10.3390/met10070876. URL https://www.mdpi.com/2075-4701/10/7/876.
[46] Ding J, Wang YD, Gulzar S, Kim YR, Underwood BS. Uncertainty quantification of simplified viscoelastic continuum damage fatigue model using the Bayesian inference-based Markov Chain Monte Carlo Method. Transport Res Rec: J Transport Res Board 2020;2674(4):247–60. https://doi.org/10.1177/0361198120910149. URL http://journals.sagepub.com/doi/10.1177/0361198120910149.
[47] Ilyani Akmar AB, Lahmer T, Bordas SPA, Beex LAA, Rabczuk T. Uncertainty quantification of dry woven fabrics: A sensitivity analysis on material properties. Compos Struct 2014;116:1–17. https://doi.org/10.1016/j.compstruct.2014.04.014. URL https://www.sciencedirect.com/science/article/pii/S0263822314001810.
[48] Bostanabad R, Liang B, Gao J, Liu WK, Cao J, Zeng D, Su X, Xu H, Li Y, Chen W. Uncertainty quantification in multiscale simulation of woven fiber composites. Comput Methods Appl Mech Eng 2018;338:506–32. https://doi.org/10.1016/j.cma.2018.04.024. URL https://www.sciencedirect.com/science/article/pii/S0045782518302032.
[49] Tao W, Zhu P, Xu C, Liu Z. Uncertainty quantification of mechanical properties for three-dimensional orthogonal woven composites. Part I: Stochastic reinforcement geometry reconstruction. Compos Struct 2020;235:111763. https://doi.org/10.1016/j.compstruct.2019.111763. URL https://www.sciencedirect.com/science/article/pii/S0263822319324948.
[50] Fernandez-Zelaia P, Lee Y, Dryepondt S, Kirka MM. Creep anisotropy modeling and uncertainty quantification of an additively manufactured Ni-based superalloy. Int J Plast 2022;151:103177. https://doi.org/10.1016/j.ijplas.2021.103177. URL https://www.sciencedirect.com/science/article/pii/S0749641921002436.
[51] Fullwood DT, Niezgoda SR, Adams BL, Kalidindi SR. Microstructure sensitive design for performance optimization. Prog Mater Sci 2010;55(6):477–562. https://doi.org/10.1016/j.pmatsci.2009.08.002. URL http://www.sciencedirect.com/science/article/pii/S0079642509000760.
[52] Gokhale AM. Experimental measurements and interpretation of microstructural N-point correlation functions. Microscopy Microanal 2004;10 (S02):736–737, publisher: Cambridge University Press. https://doi.org/10.1017/S1431927604887178. https://www.cambridge.org/core/journals/microscopy-and-microanalysis/article/experimental-measurements-and-interpretation-of-microstructural-npoint-correlation-functions/F9648F343FCD2F3503020BB9BD68AA83.
[53] Huang M. The n-point orientation correlation function and its application. Int J Solids Struct 2005;42(5):1425–41. https://doi.org/10.1016/j.ijsolstr.2004.06.037. URL https://www.sciencedirect.com/science/article/pii/S0020768304003646.
[54] Robertson AE, Kalidindi SR. Efficient generation of anisotropic N-field microstructures from 2-point statistics using multi-output Gaussian random fields. Acta Mater 2022;232:117927. https://doi.org/10.1016/j.actamat.2022.117927. URL https://www.sciencedirect.com/science/article/pii/S1359645422003093.
[55] Tewari A, Gokhale AM, Spowart JE, Miracle DB. Quantitative characterization of spatial clustering in three-dimensional microstructures using two-point correlation functions. Acta Mater 2004;52(2):307–19. https://doi.org/10.1016/j.actamat.2003.09.016. URL https://www.sciencedirect.com/science/article/pii/S1359645403005469.
[56] Torquato S. Random heterogeneous materials: microstructure and macroscopic properties. Interdisciplinary applied mathematics. New : Springer-Verlag; 2002. https://doi.org/10.1007/978-1-4757-6355-3. URL https://www.springer.com/gp/book/9780387951676.
[57] Kalidindi SR. Materials, data, and informatics. Elsevier; 2015. https://doi.org/10.1016/B978-0-12-410394-8.00001-1. URL https://linkinghub.elsevier.com/retrieve/pii/B9780124103948000011.
[58] Fast T, Niezgoda SR, Kalidindi SR. A new framework for computationally efficient structure–structure evolution linkages to facilitate high-fidelity scale bridging in multi-scale materials models. Acta Mater 2011;59 (2):699–707. https://doi.org/10.1016/j.actamat.2010.10.008. URL http://www.sciencedirect.com/science/article/pii/S1359645410006701.
[59] Kalidindi S, Niezgoda S, Landi G, Vachhani S, Fast T. A novel framework for building materials knowledge systems. Comput Mater Continua 2010;17:103–25.
[60] Cecen A, Dai H, Yabansu YC, Kalidindi SR, Song L. Material structure-property linkages using three-dimensional convolutional neural networks. Acta Mater 2018;146:76–84. https://doi.org/10.1016/j.actamat.2017.11.053. URL http://www.sciencedirect.com/science/article/pii/S1359645417310443.
[61] Çeçen A, Fast T, Kumbur EC, Kalidindi SR. A data-driven approach to establishing microstructure–property relationships in porous transport layers of polymer electrolyte fuel cells. J Power Sources 2014;245:144–53. https://doi.org/10.1016/j.jpowsour.2013.06.100. URL http://www.sciencedirect.com/science/article/pii/S0378775313011075.
[62] Gupta A, Cecen A, Goyal S, Singh AK, Kalidindi SR. Structure–property linkages using a data science approach: Application to a non-metallic inclusion/steel composite system. Acta Mater 2015;91:239–54. https://doi.org/10.1016/j.actamat.2015.02.045. URL http://www.sciencedirect.com/science/article/pii/S1359645415001603.
[63] Latypov MI, Toth LS, Kalidindi SR. Materials knowledge system for nonlinear composites. Comput Methods Appl Mech Eng 2019;346:180–96. https://doi.org/10.1016/j.cma.2018.11.034. URL http://www.sciencedirect.com/science/article/pii/S0045782518305930.
[64] Paulson NH, Priddy MW, McDowell DL, Kalidindi SR. Reduced-order microstructure-sensitive protocols to rank-order the transition fatigue resistance of polycrystalline microstructures. Int J Fatigue 2019;119:1–10. https://doi.org/10.1016/j.ijfatigue.2018.09.011. URL http://www.sciencedirect.com/science/article/pii/S0142112318305553.
[65] Paulson NH, Priddy MW, McDowell DL, Kalidindi SR. Reduced-order structure-property linkages for polycrystalline microstructures based on 2-point statistics. Acta Mater 2017;129:428–38. https://doi.org/10.1016/j.actamat.2017.03.009. URL http://www.sciencedirect.com/science/article/pii/S135964541730188X.
[66] Bock FE, Aydin RC, Cyron CJ, Huber N, Kalidindi SR, Klusemann B. A review of the application of machine learning and data mining approaches in continuum materials mechanics. Front Mater 2019;6:110. https://doi.org/10.3389/fmats.2019.00110. URL https://www.frontiersin.org/article/10.3389/fmats.2019.00110/full.
[67] Lander E, Koizumi K. Materials genome initiative strategic plan; 2021.
[68] Chaboche JL, Lesne PM, Maire JF. Continuum damage mechanics, anisotropy and damage deactivation for brittle materials like concrete and ceramic composites. Int J Damage Mech 1995;4(1):5–22, https://doi.org/10.1177/105678959500400102, publisher: SAGE Publications Ltd STM
[69] Allix O, Ladevèze P, Gilletta D, Ohayon R. A damage prediction method for composite structures. Int J Numer Meth Eng 1989;27(2):271–83. https://doi.org/10.1002/nme.1620270205. URL https://onlinelibrary.wiley.com/doi/10.1002/nme.1620270205.
[70] Ladeveze P. A damage approach for composite structures: theory and identification. in: Vautrin A, Sol H. editors. Mechanical identification of composites. Netherlands, Dordrecht: Springer; 1991, p. 44–57. https://doi.org/10.1007/978-94-011-3658-7_4.
[71] Perreux D, Oytana C. Continuum damage mechanics for microcracked composites. Compos Eng 1993;3(2):115–22. https://doi.org/10.1016/0961-9526(93)90036-J. URL https://linkinghub.elsevier.com/retrieve/pii/096195269390036J.
[72] Anderson T. Fracture mechanics, fundamentals and applications. 3rd ed. CRC Press, Taylor & Francis; 2005.
[73] Murakami S. Continuum damage mechanics, Vol. 185 of Solid Mechanics and Its Applications. Netherlands, Dordrecht: Springer; 2012. https://doi.org/10.1007/978-94-007-2666-6. http://link.springer.com/10.1007/978-94-007-2666-6.
[74] Kumar RS. Micromechanics approach for the overall elastic properties of ceramic matrix composites incorporating defect structures. American Society of Mechanical Engineers Digital Collection; 2021. https://doi.org/10.1115/GT2020-16056.
[75] Kirsch A. An introduction to the mathematical theory of inverse problems, applied mathematical sciences. New York, NY: Springer; 2011. https://doi.org/10.1007/978-1-4419-8474-6_5.
[76] Wu X, Kozlowski T, Meidani H, Shirvan K. Inverse uncertainty quantification using the modular Bayesian approach based on Gaussian process, Part 1: Theory. Nucl Eng Des 2018;335:339–55. https://doi.org/10.1016/j.nucengdes.2018.06.004. URL https://linkinghub.elsevier.com/retrieve/pii/S0029549318306423.
[77] Kennedy MC, O'Hagan A. Bayesian calibration of computer models. J Roy Stat Soc: Series B (Stat Methodol) 2001;63(3): 425–464, _eprint: https://onlinelibrary.wiley.com/doi/pdf/10.1111/1467-9868.00294. https://doi.org/10.1111/1467-9868.00294. https://onlinelibrary.wiley.com/doi/abs/10.1111/1467-9868.00294.

[78] Trucano TG, Swiler LP, Igusa T, Oberkampf WL, Pilch M. Calibration, validation, and sensitivity analysis: What's what. Reliab Eng Syst Saf 2006;91(10):1331–57. https://doi.org/10.1016/j.ress.2005.11.031. URL https://www.sciencedirect.com/science/article/pii/S0951832005002437.
[79] Goodman J, Weare J. Ensemble samplers with affine invariance. Commun Appl Mathe Comput Sci 2010;5(1):65–80. https://doi.org/10.2140/camcos.2010.5.65. URL http://msp.org/camcos/2010/5-1/p04.xhtml.
[80] Foreman-Mackey D, Hogg DW, Lang D, Goodman J. emcee: The MCMC Hammer. Publ Astron Soc Pacific 2013;125(925): 306–312, arXiv: 1202.3665. https://doi.org/10.1086/670067. http://arxiv.org/abs/1202.3665.
[81] Chontos A, Huber D, Berger TA, Kjeldsen H, Serenelli AM, Aguirre VS, et al. TESS asteroseismology of alpha mensae: benchmark ages for a G7 dwarf and its M Dwarf companion. Astrophys J 2021;922(2):229, https://doi.org/10.3847/1538-4357/ac1269. publisher: American Astronomical Society.
[82] Huang S, Yin H, Hu S, Chen X, Jiang Y, Alexeeva S. The X-Ray Outburst of PG 1553$\mathplus$113: A precession effect of two jets in the supermassive black hole binary system, Astrophys J2021;922(2): 222, https://doi.org/10.3847/1538-4357/ac2d98. publisher: American Astronomical Society.
[83] Suárez Mascareño A, Damasso V, Lodieu N, Sozzetti A, Béjar VJS, Benatti V, Zapatero Osorio MR, et al. Rapid contraction of giant planets orbiting the 20-million-year-old star V1298 Tau. Nat Astron (2021) 1–9Bandiera_abtest: a Cg_type: Nature Research Journals Primary_atype: Research Publisher: Nature Publishing Group Subject_term: Exoplanets;Stars Subject_term_id: exoplanets;stars. https://doi.org/10.1038/s41550-021-01533-7. https://www.nature.com/articles/s41550-021-01533-7.
[84] Mak S, Joseph VR. Support points. Ann Stat 46(6A);2018. https://doi.org/10.1214/17-AOS1629. https://projecteuclid.org/journals/annals-of-statistics/volume-46/issue-6A/Support-points/10.1214/17-AOS1629.full.
[85] Székely GJ, Rizzo ML. Energy statistics: A class of statistics based on distances. J Stat Plann Inference 2013;143(8):1249–72. https://doi.org/10.1016/j.jspi.2013.03.018. URL https://www.sciencedirect.com/science/article/pii/S0378375813000633.
[86] Vakayil A, Joseph VR. Data Twinning. Stat Anal Data Min: The ASA Data Sci J. 2022 sam.11574ArXiv:2110.02927 [cs, stat]. https://doi.org/10.1002/sam.11574. http://arxiv.org/abs/2110.02927.
[87] Niezgoda SR, Fullwood DT, Kalidindi SR. Delineation of the space of 2-point correlations in a composite material system. Acta Mater 2008;56(18):5285–92. https://doi.org/10.1016/j.actamat.2008.07.005. URL http://www.sciencedirect.com/science/article/pii/S1359645408004886.
[88] Fernandez-Zelaia P, Yabansu YC, Kalidindi SR. A comparative study of the efficacy of local/global and parametric/nonparametric machine learning methods for establishing structure-property linkages in high-contrast 3D elastic composites. Integrat Mater Manuf Innovat 2019;8(2):67–81. https://doi.org/10.1007/s40192-019-00129-4.
[89] Yabansu YC, Altschuh P, Hötzer J, Selzer M, Nestler B, Kalidindi SR. A digital workflow for learning the reduced-order structure-property linkages for permeability of porous membranes. Acta Mater 2020;195:668–80. https://doi.org/10.1016/j.actamat.2020.06.003. URL http://www.sciencedirect.com/science/article/pii/S1359645420304274.
[90] Yabansu YC, Steinmetz P, Hötzer J, Kalidindi SR, Nestler B. Extraction of reduced-order process-structure linkages from phase-field simulations. Acta Mater 2017;124:182–94. https://doi.org/10.1016/j.actamat.2016.10.071. URL http://www.sciencedirect.com/science/article/pii/S1359645416308485.
[91] Niezgoda SR, Kanjarla AK, Kalidindi SR. Novel microstructure quantification framework for databasing, visualization, and analysis of microstructure data. Integrat Mater Manuf Innovat 2013;2(1):54–80. https://doi.org/10.1186/2193-9772-2-3.
[92] Rasmussen CE, Williams CKI. Gaussian processes for machine learning, Adaptive computation and machine learning. Cambridge, Mass: MIT Press; 2006. oCLC: ocm61285753.
[93] Titsias MK. Variational learning of inducing variables in sparse Gaussian processes ;2009: 8.
[94] Alvarez MA, Rosasco L, Lawrence ND. Kernels for Vector-Valued Functions: a Review, number: arXiv:1106.6251 arXiv:1106.6251 [cs, math, stat] (Apr. 2012). URL http://arxiv.org/abs/1106.6251.
[95] Lázaro-Gredilla M, Figueiras-Vidal A. Inter-domain Gaussian Processes for sparse inference using inducing features. In: Advances in Neural Information Processing Systems, vol. 22, Curran Associates Inc, 2009. https://proceedings.neurips.cc/paper/2009/hash/5ea1649a31336092c05438df996a3e59-Abstract.html.
[96] Journel AG, Huijbregts CJ. Mining Geostatistics. Blackburn Press; 2003. google-Books-ID: Id1GAAAAYAAJ.
[97] Iskakov A, Kalidindi SR. A framework for the systematic design of segmentation workflows. Integrat Mater Manuf Innovat 2020;9(1):70–88. https://doi.org/10.1007/s40192-019-00166-z.
[98] MATLAB, version 9.11 (R2021b), The MathWorks Inc., Natick, Massachusetts, 2021.
[99] Naik RA. Failure analysis of woven and braided fabric reinforced composites. J Compos Mater 1995;29(17):2334–63. https://doi.org/10.1177/002199839502901706. URL http://journals.sagepub.com/doi/10.1177/002199839502901706.
[100] Lin H, Brown LP, Long AC. Modelling and simulating textile structures using TexGen. Adv Mater Res 2011;331:44–7. https://doi.org/10.4028/www.scientific.net/AMR.331.44. URL https://www.scientific.net/AMR.331.44.
[101] Murthy P, Mital S, DiCarlo A. Characterizing the properties of a Woven SiC/SiC composite using W-CEMCAN computer code, Tech. Rep. NASA/TM-1999-209173; 1999.
[102] Lang J, DiCarlo J. Design curve generation for 3D SiC fiber architecture; Jan. 2014.
[103] Dassault S. Abaqus/CAE User's Manual, 1174; 2019.
[104] Kim HJ, Swan CC. Voxel-based meshing and unit-cell analysis of textile composites. Int J Num Methods Eng 2003;56(7) 977–1006, _eprint: https://onlinelibrary.wiley.com/doi/pdf/10.1002/nme.594. https://doi.org/10.1002/nme.594. https://onlinelibrary.wiley.com/doi/abs/10.1002/nme.594.
[105] Ma D, Manes A, Giglio M. The effect of mesh morphologies on the mesoscale Finite Element modelling of woven composites. Proc Struct Integ 2019;24:80–90. https://doi.org/10.1016/j.prostr.2020.02.007. URL https://linkinghub.elsevier.com/retrieve/pii/S2452321620302304.
[106] Marshall A, Kalidindi SR. Autonomous development of a machine-learning model for the plastic response of two-phase composites from micromechanical finite element models. JOM 2021;73(7):2085–95. https://doi.org/10.1007/s11837-021-04696-w.
[107] Generale AP, Kalidindi SR. Reduced-order models for microstructure-sensitive effective thermal conductivity of woven ceramic matrix composites with residual porosity. Compos Struct 2021;274:114399. https://doi.org/10.1016/j.compstruct.2021.114399. URL https://linkinghub.elsevier.com/retrieve/pii/S0263822321008618.
[108] Fernandez-Zelaia P, Melkote SN. Process-structure-property modeling for severe plastic deformation processes using orientation imaging microscopy and data-driven techniques. Integrat Mater Manuf Innovat 2019;8(1):17–36. https://doi.org/10.1007/s40192-019-00125-8.
[109] Gomberg JA, Medford AJ, Kalidindi SR. Extracting knowledge from molecular mechanics simulations of grain boundaries using machine learning. Acta Mater 2017;133:100–8. https://doi.org/10.1016/j.actamat.2017.05.009. URL https://www.sciencedirect.com/science/article/pii/S1359645417303865.
[110] Iskakov A, Yabansu YC, Rajagopalan S, Kapustina A, Kalidindi SR. Application of spherical indentation and the materials knowledge system framework to establishing microstructure-yield strength linkages from carbon steel scoops excised from high-temperature exposed components. Acta Mater 2018;144:758–67. https://doi.org/10.1016/j.actamat.2017.11.024. URL https://www.sciencedirect.com/science/article/pii/S1359645417309679.
[111] Moure MM, Sanchez-Saez S, Barbero E, Barbero EJ. Analysis of damage localization in composite laminates using a discrete damage model. Compos Part B: Eng 2014;66:224–32. https://doi.org/10.1016/j.compositesb.2014.05.015. URL https://www.sciencedirect.com/science/article/pii/S1359836814002133.
[112] Landi G, Niezgoda S, Kalidindi S. Multi-scale modeling of elastic response of three-dimensional voxel-based microstructure datasets using novel DFT-based knowledge systems. Acta Mater 2010;58:2716–25. https://doi.org/10.1016/j.actamat.2010.01.007.
[113] Li S, Wongsto A. Unit cells for micromechanical analyses of particle-reinforced composites. Mech Mater 2004;30.
[114] Tsukrov I, Piat R, Novak J, Schnack E. Micromechanical modeling of porous carbon/carbon composites. Mech Adv Mater Struct 2005;12(1):43–54. https://doi.org/10.1080/15376490490492034. publisher: Taylor & Francis _eprint: https://doi.org/10.1080/15376490490492034. URL https://doi.org/10.1080/15376490490492034.
[115] Tian W, Qi L, Chao X, Liang J, Fu M. Periodic boundary condition and its numerical implementation algorithm for the evaluation of effective mechanical properties of the composites with complicated micro-structures. Compos Part B: Eng 2019;162:1–10. https://doi.org/10.1016/j.compositesb.2018.10.053. URL https://www.sciencedirect.com/science/article/pii/S1359836818319838.
[116] Chao X, Qi L, Cheng J, Tian W, Zhang S, Li H. Numerical evaluation of the effect of pores on effective elastic properties of carbon/carbon composites. Compos Struct 2018;196:108–16. https://doi.org/10.1016/j.compstruct.2018.05.014. URL https://www.sciencedirect.com/science/article/pii/S0263822317336619.
[117] Genet M, Marcin L, Baranger E, Cluzel C, Ladevèze P, Mouret A. Computational prediction of the lifetime of self-healing CMC structures. Compos Part A: Appl Sci Manuf 2012;43(2):294–303. https://doi.org/10.1016/j.compositesa.2011.11.004. URL https://linkinghub.elsevier.com/retrieve/pii/S1359835X11003757.
[118] DeRienzo JM. Bi-axial (tension-torsion) testing of an oxide/oxide ceramic matrix composite. Air Force Institute of Technology; 2013. Ph.D. thesis.
[119] Flores S, Evans AG, Zok FW, Genet M, Cox B, Marshall D, Sudre O, Yang Q. Treating matrix nonlinearity in the binary model formulation for 3D ceramic composite structures. Compos Part A: Appl Sci Manuf 2010;41(2):222–9. https://doi.org/10.1016/j.compositesa.2009.10.020. URL https://www.sciencedirect.com/science/article/pii/S1359835X09003455.
[120] Miot S, Hochard C, Lahellec N. A non-local criterion for modelling unbalanced woven ply laminates with stress concentrations. Compos Struct 2010;92(7):1574–80. https://doi.org/10.1016/j.compstruct.2009.11.019. URL https://www.sciencedirect.com/science/article/pii/S0263822309004887.
[121] Hochard C, Lahellec N, Bordreuil C. A ply scale non-local fibre rupture criterion for CFRP woven ply laminated structures. Compos Struct 2007;80(3):321–6. https://doi.org/10.1016/j.compstruct.2006.05.021. URL https://www.sciencedirect.com/science/article/pii/S0263822306002285.
[122] Castillo AR, Kalidindi SR. Bayesian estimation of single ply anisotropic elastic constants from spherical indentations on multi-laminate polymer-matrix

fiber-reinforced composite samples. Meccanica https://doi.org/10.1007/s11012-020-01154-w. http://link.springer.com/10.1007/s11012-020-01154-w.
[123] Strang G. Introduction to linear algebra. 5th ed. Wellesley: Wellesley-Cambridge Press; 2016.
[124] Wold S, Esbensen K, Geladi P. Principal component analysis. Chemomet Intell Lab Syst 1987;2(1):37–52. https://doi.org/10.1016/0169-7439(87)80084-9. URL https://www.sciencedirect.com/science/article/pii/0169743987800849.
[125] McKay MD, Beckman RJ, Conover WJ. A comparison of three methods for selecting values of input variables in the analysis of output from a computer code. Technometrics 1979;21(2):239–245, https://doi.org/10.2307/1268522. https://www.jstor.org/stable/1268522 publisher: [Taylor & Francis Ltd, American Statistical Association, American Society for Quality].
[126] Joseph VR, Gul E, Ba S. Maximum projection designs for computer experiments. Biometrika 2015;102(2):371–380, publisher: [Oxford University Press, Biometrika Trust]. https://www.jstor.org/stable/43908541.
[127] Ruder S. An overview of gradient descent optimization algorithms, number: arXiv:1609.04747 arXiv:1609.04747 [cs] (Jun. 2017). http://arxiv.org/abs/1609.04747.
[128] Almansour AS. of the requirements for the degree. University of Akron; 2017. Ph.D. thesis.
[129] Jacques S, Lopez-Marure A, Vincent C, Vincent H, Bouix J. SiC/SiC minicomposites with structure-graded BN interphases. J Eur Ceram Soc 2000;20(12):1929–38. https://doi.org/10.1016/S0955-2219(00)00064-9. URL https://linkinghub.elsevier.com/retrieve/pii/S0955221900000649.
[130] Foreman-Mackey D. corner.py: Scatterplot matrices in Python. J Open Source Softw 2016;1(2):24. https://doi.org/10.21105/joss.00024. URL https://joss.theoj.org/papers/10.21105/joss.00024.
[131] Seeger MW, Williams CKI, Lawrence ND. Fast forward selection to speed up sparse Gaussian process regression. In: International Workshop on Artificial Intelligence and Statistics, PMLR; 2003, pp. 254–261, iSSN: 2640–3498. https://proceedings.mlr.press/r4/seeger03a.html.
[132] Snelson E, Ghahramani Z. Sparse Gaussian Processes using Pseudo-inputs. In: Proceedings of the ninth international workshop on artificial intelligence and statistics; 2003, p. 8.
[133] Bui TD, Yan J, Turner RE. A Unifying framework for gaussian process pseudo-point approximations using power expectation propagation, arXiv:1605.07066 [cs, stat] (Oct. 2017). https://doi.org/10.48550/arXiv.1605.07066. http://arxiv.org/abs/1605.07066.